Nfib regulates progenitor competence in maturation of GABAergic neurons

Yana Kotlyarenko[1,2,+], Ann Rose Bright [1,2,+], Florian Neuhaus[1,2], Diana Rodrigues [1,3], Ilaria Vitali[1,2], Michael H. Myoga [1,2,3], and Christian Mayer [1,2,*]

[1]Max Planck Institute for Biological Intelligence, Martinsried, 82152, Germany
[2]Max Planck Institute of Neurobiology, Martinsried, 82152, Germany
[3]Biomedical Center, Ludwig-Maximilians-Universität, Martinsried, 82152, Germany

Abstract

Inhibitory neurons of the telencephalon are generated from progenitors in the ganglionic eminences that mature and differentiate into specialized cell types. Here, we used single cell transcriptomics and single cell chromatin accessibility together with lineage tracing and birthdating techniques to investigate the influence of progenitor competence on the development of GABAergic precursors. We found that the timing of neurogenesis influences the maturation competence of progenitors to develop towards a fully functional state, but not their differentiation competence to evolve into transcriptomically diverse states. The underlying mechanism defining maturation competence was chromatin priming, orchestrated by the transcription factor Nfib in collaboration with regulators of inhibitory neuron development. Finally, transplantation experiments revealed an interplay between both intrinsic and extrinsic cues acting upon maturation competence. These findings identify a mechanism that coordinates inhibitory neuron development by changing its maturation to achieve maximum adaptability to their environment.

Keywords— GABAergic neurons, ganglionic eminence, development, progenitors, differentiation, maturation, competence, chromatin priming

Introduction

The development of diverse neuronal types is orchestrated with temporal, spatial, and numerical precision. This process is influenced by the competence of neuronal progenitor cells, which can be linked to various regulatory programs, including those governing cell differentiation and maturation (Bonnefont and Vanderhaeghen, 2021; Farnsworth and Doe, 2017). Excitatory neurons of the mammalian cerebral cortex are developmentally derived from proliferative zones in the dorsal telencephalon (Puelles et al., 2000). Several studies indicated a pronounced temporal change in the progenitor competence that dictates the sequence of neuronal differentiation events and guides newborn neurons toward their final fate (Di Bella et al., 2021; Telley et al., 2019; Vitali et al., 2018). Inhibitory neurons, by contrast, are developmentally derived from proliferative zones in the ventral telencephalon, called the ganglionic eminences (GE) (Anderson et al., 2001; Marín and Rubenstein, 2001; Corbin et al., 2001; Wonders and Anderson, 2006; Flames et al., 2007; Wonders et al., 2008; Gelman et al., 2011; Kelly et al., 2018). The gene expression signatures of precursor states of inhibitory neurons emerge shortly after cell cycle exit and before neuronal precursors migrate to their final positions in different structures of the telencephalon, including the cerebral cortex and striatum (Mayer et al., 2018; Mi et al., 2018). A clonal analysis with heritable DNA tags showed that during peak neurogenesis, individual mitotic progenitor cells in the GE possess the competence to generate inhibitory neurons with diverse transcriptomic signatures (Bandler et al., 2022). While there has been progress in correlating gene expression dynamics with chromatin accessibility (Allaway et al., 2021; Fleck et al., 2021; Janssens et al., 2021; Gonzalez-Blas et al., 2023), the impact of mitotic progenitor competence on the differentiation and maturation of inhibitory neurons remains poorly understood.

Here, we explored the role of progenitor competence in the development of inhibitory neurons using a multi-faceted approach. This involved single-cell RNA sequencing (scRNA-seq), single-cell analysis of accessible chromatin (scATAC-seq), barcode lineage-tracing (TrackerSeq), neuronal birthdating (FlashTag) and heterochronic transplantation. A comparison of isochronic cohorts of

early and late born inhibitory neuron precursors showed that individual progenitors within the GE maintain their competence to generate postmitotic precursors that differentiate into a consistent set of cell states. However, early and late born cohorts differ in the progression rate at which they move through maturation. We propose that these stage-specific differences originate from variations in chromatin accessibility patterns. Support for this hypothesis was provided by a gene regulatory network (GRN) established by overlaying the scRNA-seq and scATAC-seq data, which revealed transcription factor (TF) modules exclusively active in late born progenitors that could underlay the changes in competence. Finally, heterochronic transplantations revealed that the maturation competence is also influenced by the extrinsic environment. These findings elucidate that both maturation and differentiation competence of progenitors influence neuronal development, but their relative contributions differ between dorsal and ventral lineages.

Results

To investigate the relationship between progenitor competence and neuronal maturation and differentiation in GABAergic lineages, we compared the neuronal output at different stages of neurogenesis (embryonic day 12.5–16.5; e12.5–e16.5) by combining numerous methods to target progenitors, including scRNA-seq (⋆), barcode lineage tracing (▲) and fluorescent birthdating (■; Fig. 1a,b, Fig. S1a,b). For scRNA-seq (⋆), GE from e12.5, e14.5, and e16.5 Dlx5/6-Cre::tdTomato mouse embryos, which fate-map GABAergic neurons (Monory et al., 2006), were manually dissected and dissociated. From the same brains, cortical and striatal regions were collected and tdTomato positive (tdTomato$^+$) cells were enriched by fluorescence-activated cell sorting (FACS). Cells from the GE and tdTomato$^+$ cells from the cortex and striatum were pooled to capture developmental states ranging from mitotic progenitors to postmitotic precursors and subjected to scRNA-seq (Fig. S1c). For barcode lineage tracing (▲), we devised a published method called TrackerSeq, which uses heritable DNA barcodes to label individual progenitors and their progeny followed by multiplexed scRNA-seq (Bandler et al., 2022). We targeted progenitors in the GE at e16.5 with

TrackerSeq plasmids via *in utero* electroporation (IUE), FACS-enriched electroporated cells 96 h later, and performed scRNA-seq (TrackerSeq$_{e16.5+96h}$). In our analysis, we also included a published TrackerSeq dataset (Bandler et al., 2022), in which TrackerSeq plasmids were electroporated at e12.5, and the targeted cells were collected 96 h later (TrackerSeq$_{e12.5+96h}$) (Fig. S1d). For birthdating (■), we used a technique called FlashTag (FT), which labels isochronic cohorts of cells with the fluorescent dye carboxyfluorescein succinimidyl ester (CFSE) (Govindan et al., 2018). In this method, mitotic cells layering the ventricle are labelled during the M phase of the cell cycle and maintain high fluorescence when leaving the cell cycle. We injected CFSE into the ventricles of e12.5 and e16.5 wild-type embryos, and anatomically dissected the GE six h later, to FACS enrich FT labelled (FT$^+$) cells and perform scRNA-seq (FT$_{e12.5+6h}$ and FT$_{e16.5+6h}$ respectively). We also injected CFSE into the ventricles of e12.5 Dlx5/6-Cre::tdTomato mouse embryos and collected inhibitory neurons after migration from anatomically dissected cortex and striatum at 96 h post injection. TdTomato$^+$ and FT$^+$ cells were enriched by FACS and scRNA-seq was performed (FT$_{e12.5+96h}$; Fig. S1e,f,g).

We pre-processed and merged datasets from all three methods (⋆, ▲, ■), using Seurat (Stuart et al., 2019), aligned the batches using Monocle3, and projected the data into a low-dimensional UMAP space (Fig. 1c) (Trapnell et al., 2014; Haghverdi et al., 2018). We then performed clustering (Fig. 1d,Fig. S2a,b) and trajectory (Fig. S2c) analyses using Monocle3, which learns the sequence of gene expression changes and uses a diffusion pseudotime algorithm to identify developmental trajectories. Consistent with previous work, clusters and trajectories represented a continuum of cell state transitions during cellular maturation and differentiation (Fig. S2d) (Mayer et al., 2018; Bandler et al., 2022; Lee et al., 2022; Rhodes et al., 2022; Lim et al., 2018). We manually annotated clusters based on marker gene expression, identifying them as mitotic apical progenitors (APs; Fabp7), mitotic basal progenitors (BPs; Fabp7/Ccnd1, Top2a, and Ube2c), GABAergic projection neuron precursors (PNs: Abracl, Tshz1, Six3/Gucy1a3, Gucy1a3, and Ebf1/Isl1), and GABAergic interneuron precursors (INs: Nkx2-1, Npy, Maf/Sst, and Snhg11; Fig. 1d, Fig. S2f). After cell cycle exit, a common trajectory diverged, giving rise to distinct precursor states of GABAergic PNs and

INs. Each of these trajectories underwent subsequent divisions, resulting in multiple postmitotic precursor states that could be linked to adult cell types (Mayer et al., 2018; Bandler et al., 2022) (Fig. S2f,e).

The differentiation competence differs between dorsal and ventral lineages

To dissect neuronal maturation and differentiation during early stages of development, we first explored the scRNA-seq (⋆) data in our combined single cell trajectory (Fig. 1e) and calculated the sequential patterns of gene expression along the Monocle3 pseudotime trajectory. Surprisingly, the expression of TFs that progressed along the trajectory was highly conserved across different stages of neurogenesis (e12.5, e14.5 and e16.5; Fig. S3a). This developmental pattern differs from previous observations in dorsal lineages (Di Bella et al., 2021; Telley et al., 2019).

Therefore, before delving further into our combined dataset, we explored dorsal and ventral lineages by projecting them into the same subspace. We merged and aligned our scRNA-seq (⋆) datasets with published data of GABAergic neurons from e13.5 and e15.5 (Bandler et al., 2022) and with data of glutamatergic neurons from e12.5 to e16.5 (Di Bella et al., 2021) using Monocle3 (Fig. 1f, Fig. S3b). On the UMAP plot, dorsal and ventral lineages were in proximity at the level of APs, and dispersed into different directions at more mature cell states, i.e. BPs and postmitotic precursors (Fig. S3c) (Moreau et al., 2021). When comparing successive developmental stages, cells of the dorsal lineage showed a sequential shift in the UMAP positioning, consistent with findings from previous studies (Telley et al., 2016; Di Bella et al., 2021). In contrast, cells of the ventral lineage largely overlapped across developmental stages (Fig. 1f). We inferred genes that describe the emergence of inhibitory and excitatory neurons by selecting dynamic genes across pseudotime in the two lineages (methods). We found few genes overlapping between inhibitory and excitatory lineages, primarily at initial pseudotime scores (Fig. S3d,e; Fig. S4a–d).

To quantify the temporal progression of dorsal and ventral progenitors, we calculated Pearson correlation coefficients between mitotic groups based on highly variable genes. Ventral progenitors showed higher correlation coefficients between successive stages of neurogenesis than dorsal

progenitors, indicating generally less change in their gene expression profiles (Fig. 1g). Furthermore, differential gene expression analysis of ventral progenitors across stages revealed that only a few genes were upregulated at later stages of neurogenesis (Fig. S5a). Genes that were downregulated at later stages were primarily related to self-renewal (Fig. S5a,b), in line with a change in balance between cell proliferation and differentiation during neurogenesis (Götz and Huttner, 2005).

Next, we annotated postmitotic cells based on marker gene expression (ventral lineage) or published data (dorsal lineage, (Di Bella et al., 2021)) and quantified the proportion of cells in postmitotic precursor states across different developmental stages (Fig. S5c). While the relative distribution of precursor states was similar across stages in ventral cells, it sequentially shifted in dorsal cells (SCPN → CThPN → DL CPN → UP CPN; Fig. 1h). Taken together, our observations suggest that the differentiation competence of GABAergic progenitors is stable throughout neurogenesis, and the generation of GABAergic precursor states does not adhere to a stage-specific sequence. This contrasts the sequential generation of precursor states in dorsal lineages.

Clonal divergence is maintained across neurogenesis

Our results so far suggest that, at the population level, progenitors in the GE can give rise to a similar set of precursor states throughout neurogenesis. To investigate whether the clonal progeny of individual progenitors can diverge into distinct precursor states, we next analysed the barcode lineage tracing (▲) data in our combined single cell trajectory (Fig. 1i). We selected multicellular clones with cells in the branch tips of the Monocle3 trajectory (Fig. 1j–l, Fig. S6a–d) and grouped them according to whether their members were distributed in one (non-dispersing clones) or several (dispersing clones) branch tips. Consistent with Bandler *et al.*, a subset of the $\text{TrackerSeq}_{\text{e12.5 + 96h}}$ clones dispersed into multiple branch tips. Notably, a comparable fraction of dispersing clones was found in $\text{TrackerSeq}_{\text{e16.5 + 96h}}$ (Fig. 1k, l, m). The true proportion of dispersing clones is likely higher than observed, as TrackerSeq only partially recovers clones due to substantial cell loss during sample preparation (Bandler et al., 2022). Clonal resolution enables linking individual mitotic progenitor cells to the fate of their postmitotic progeny. We tested whether the transcriptome of

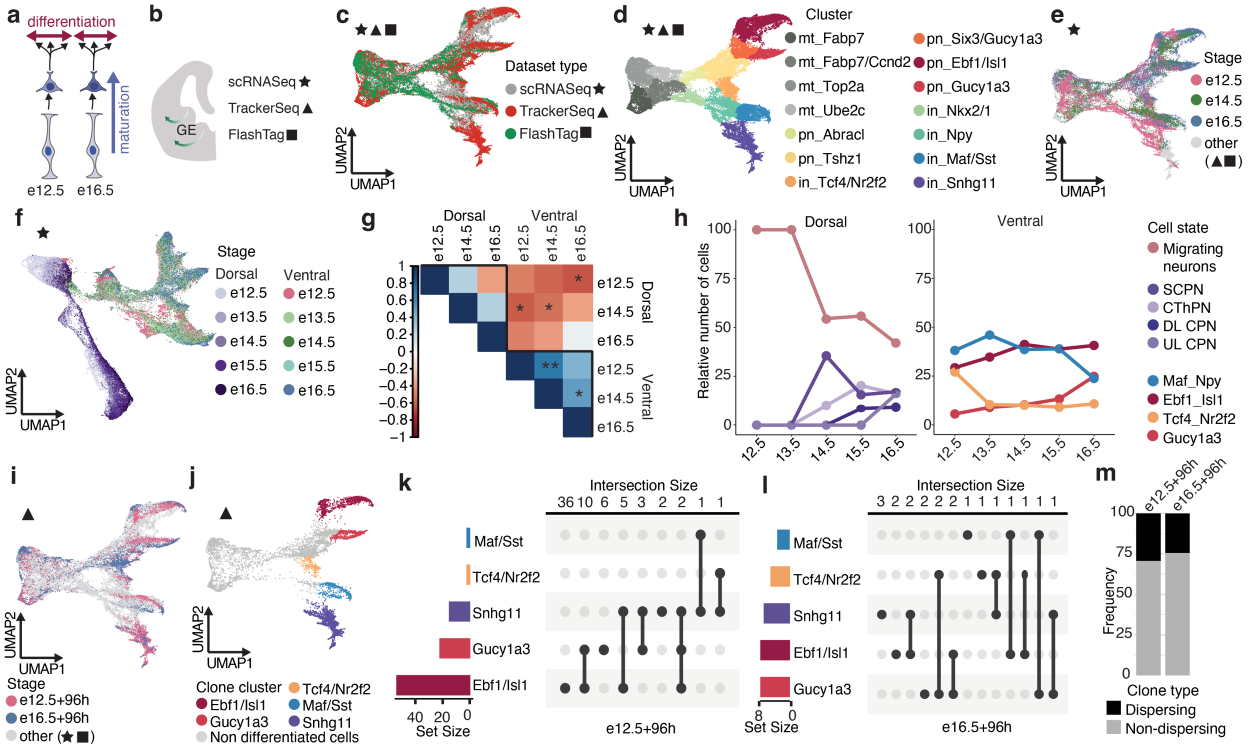

Figure 1: Stable differentiation competence in GABAergic progenitors. **a**, Schematic illustrating the difference between maturation and differentiation. **b**, Summary of methods used to investigate the competence of progenitors located in the ganglionic eminences (GE). **c**, UMAP plot depicting single cells derived from scRNAseq, TrackerSeq, and FlashTag datasets aligned in Monocle3; Different symbols and colours corresponding to dataset. **d**, UMAP plot showing GABAergic cells, each colour representing a different cluster. Clusters are annotated based on top marker genes and broad cluster identity (mt: mitotic, pn: projection neuron, in: interneuron). **e**, UMAP plot showing scRNAseq datasets, with colours indicating various collection stages. **f**, UMAP plot showing single cells from ventral (GABAergic lineage) and dorsal (glutamatergic lineage) telencephalon, with colours indicating various collection stages. **g**, Pearson's correlation plot between dorsal and ventral progenitors at different developmental stages; * P¡0.05, ** P¡0.01. **h**, Line plot showing relative cell number of dorsal (left) and ventral (right) postmitotic neuronal states across stages. The annotation of dorsal cell states is derived from the original publication. SCPN: subcerebral projection neuron, CThPN: corticothalamic projection neuron, DL CPN: deep layer callosal projection neuron, UL CPN: upper layer callosal projection neuron. **i**, UMAP plot showing TrackerSeq barcoded cells, each colour representing a stage of IUE; IUE at e12.5 and e16.5, scRNA-seq after 96 hours. **j**, UMAP plot showing cell states at the branches, used to group clones. **k**, Upset plot showing clonal intersections in $\text{TrackerSeq}_{\text{e12.5 + 96h}}$. **l**, Upset plot showing clonal intersections in $\text{TrackerSeq}_{\text{e16.5 + 96h}}$. **m**, Barplot showing the frequency of dispersing and non-dispersing clones in $\text{TrackerSeq}_{\text{e12.5 + 96h}}$ and $\text{TrackerSeq}_{\text{e16.5 + 96h}}$.

mitotic cells correlates to the transcriptome of their postmitotic sister cells (methods). Interestingly, mitotic progenitor cells that were part of non-dispersing clones did not correlate more strongly with their clonal output than did randomly selected progenitor cells (Fig. S7a–d). Overall, the clonal analysis indicates that progenitor cells maintained a stable level of differentiation competence throughout neurogenesis, a conclusion that aligns with the results of the population level analysis.

Maturation dynamics differ between early and late born neurons

Next, we examined the maturation and differentiation of postmitotic cells at different stages of neurogenesis, using the fluorescent birthdating (■) data in our combined single-cell trajectory (Fig. 2a). FT^+ cohorts collected six hours after CFSE application ($FT_{e12.5+6h}$ and $FT_{e16.5+6h}$) contained mitotic progenitors as well as early postmitotic neuronal precursors. Ninety-six hours after CFSE application ($FT_{e12.5+96h}$), FT^+ cohorts contained exclusively postmitotic cells (Fig. S8a), consistent with the notion that FT marks isochronic cohorts of cells that exit the cell cycle shortly after CFSE application (Telley et al., 2016; Mayer et al., 2018). Notably, the postmitotic fraction of all three conditions ($FT_{e12.5+6h}$, $FT_{e12.5+96h}$, $FT_{e16.5+6h}$) differentiated into all precursor states, albeit in different proportions (Fig. 2b). Next, we quantified the Monocle3 pseudotime (PT) scores as a proxy for the degree of maturation acquired by the different FT^+ cohorts. As expected, given its later collection, $FT_{e12.5+96h}$ showed higher PT scores than $FT_{e12.5+6h}$. Strikingly, the PT score of $FT_{e16.5+6h}$ was markedly higher than that of $FT_{e12.5+6h}$, even though both were collected after six hours (Fig. 2c). Next, we performed a differential gene expression (DGE) analysis between postmitotic cells of the six h cohorts ($FT_{e12.5+6h}$ vs. $FT_{e16.5+6h}$; Fig. 2d). Genes upregulated in $FT_{e16.5+6h}$ overlapped with the gene expression found in $FT_{e12.5+96h}$ (Fig. 2e, Fig. S8b). This suggests that late born neurons reach a similar gene expression profile within six hours as early born neurons within 96 hours. Many of the genes upregulated in $FT_{e16.5+6h}$ were associated with the promotion of neuronal proliferation and migration (Table S1). Some of these genes were specifically linked to neuronal signalling pathways. Overall, our results using FT birthdating suggest that although newborn neurons at different stages differentiate similarly into precursor states, they differ

in their maturation dynamics.

The observed maturational shift in GABAergic neuronal output during neurogenesis may serve to adapt newly born neurons to the differences in time available for migration and network integration between early and late born neurons. To test this hypothesis, we developed a genetic mouse model for temporal cohort labelling that allows comparison of the functional properties of early and late born neurons at postnatal day 8 (P8; Fig. S9). By focusing on striatal projection neurons, we observed that the $TX_{e12.5}$ and $TX_{e16.5}$ born cohorts still displayed morphological and electrophysiological differences at P8 (Fig. S10). Thus, the differences had not been fully compensated by this time, and we were unable to definitively confirm the hypothesis.

Maturation shift is paralleled by changes in chromatin accessibility

To explore whether the different maturation dynamics we observed at embryonic stages are associated with changes at the chromatin level, we profiled single-cell chromatin accessibility using the assay for transposase-accessible chromatin using sequencing (scATAC–seq; (Buenrostro et al., 2015)) on samples derived from FT^+ cohorts in the GE (Fig. S11a). We injected CFSE into the ventricles of e12.5 and e16.5 wild-type embryos, anatomically dissected the GE six h later ($FT_{e12.5+6h}$, $FT_{e16.5+6h}$, respectively), enriched FT^+ cells via FACS, and performed scATAC-seq (Fig. S11b). Following sequencing, we mapped the paired-end reads to a mm10 reference genome and employed the ArchR framework (Granja et al., 2021) for quality control, as well as data processing steps such as dimensionality reduction, clustering, and peak calling. Cell annotations were determined based on gene body accessibility patterns of cell state marker genes (Fig. 2f and Fig. S11c).

In contrast to the isochronic cohorts observed in the scRNA-seq experiments (Fig. 1e), $FT_{e12.5+6h}$ and $FT_{e16.5+6h}$ in the scATAC-seq experiment were separate on the UMAP plot, both in mitotic and postmitotic cell states (Fig. 2f). To identify and quantify the cis-regulatory elements (CREs) responsible for this separation, we independently conducted peak calling on $FT_{e12.5+6h}$ and $FT_{e16.5+6h}$. We then categorized the resulting peaks to identify genomic sites with e12.5-specific peaks, e16.5-specific peaks, and sites with overlapping peaks (”e12.5-sites”, ”e16.5-sites” and

”overlapping-sites”, respectively; Fig. S11d). Subsequently, we computed the ATAC-seq fragment distribution and displayed the results in coverage plots. At e12.5-sites, we observed higher accessibility in $FT_{e12.5+6h}$ than in $FT_{e16.5+6h}$. Conversely, e16.5-sites had higher accessibility in $FT_{e16.5+6h}$ than $FT_{e12.5+6h}$ (Fig. 2g). The peak sets were divided by genomic region into promoters, distal, exonic, and intergenic regions (Fig. S11e). At e12.5-sites and e16.5-sites, distal and intergenic regions represented the largest proportion of peaks. Together, this indicates that the chromatin accessibility undergoes marked changes between different stages of development, implying a dynamic process of chromatin remodelling that predominantly occurs at distal and intronic regulatory elements. To define the functional status of identified sites as poised-active distal regulatory elements, we analysed the distribution of H3K4me1 fragments, a well-established enhancer mark (Heintzman et al., 2007), utilizing forebrain ChIP-seq data from ENCODE (Gorkin et al., 2020). H3K4me1 profiles closely aligned with chromatin accessibility profiles (Fig. 2g). Specifically, e12.5-sites exhibited a stronger H3K4me1 signal at e12.5 compared to e16.5, and the contrary was observed for e16.5-sites. These observations suggest that distal regulatory elements are potentially maintained in a poised-active state and likely drive the stage-specific dynamics in chromatin accessibility.

To explore how the stage-specific accessibility of CREs relates to the maturation process, we assigned a PT score to cells along a maturation trajectory (from APs to BPs to precursor cells; Fig. 2h). We performed peak calling along the inferred trajectory and grouped the identified CREs into three main categories based on their accessibility profiles along the pseudotime: ”initial”, ”intermediate”, and ”late” CREs, corresponding broadly to APs, BPs, and precursor cells. We found more peaks in ”initial” CREs at $FT_{e16.5+6h}$ in respect to $FT_{e12.5+6h}$, suggesting an early opening of additional regulatory elements in e16.5 progenitors (Fig. S11f). To identify associated TFs, we subsequently conducted motif scanning on the peaks that were specific to the ”initial”, ”intermediate”, and ”late” CREs at both stages. From this analysis, we identified both common and stage-specific motifs (Fig. 2h). Motifs of TFs associated with inhibitory neuron development, such as Tcf4, Meis2, Ebf1, and Isl1 (Fig. S3a), were detected at both stages. Conversely, several motifs

from the NFI family (Nfia, Nfib, Nfic) were linked exclusively to ”initial” CREs in $FT_{e16.5+6h}$. The NFI TFs are known for regulating key steps during brain development (Zenker et al., 2019), such as neural and glial cell differentiation (Bunt et al., 2017), neuronal migration (Heng et al., 2012), and maturation (Hickey et al., 2019).

DNA-binding proteins, like TFs, protect genomic regions from Tn5 integration during ATAC-seq sample preparation, creating a measurable ”footprint” that reflects the binding patterns of TFs on chromatin. These footprints, thus predict the strength of TF binding (i.e. TF activity) and binding locations. We conducted a footprint analysis on the FT^+ cohorts, using TOBIAS (Bentsen et al., 2020), and performed differential binding analysis. Among the differential factors, the NFI family demonstrated the most substantial and statistically significant increase of TF binding activity in $FT_{e16.5+6h}$ (Fig. S11g). To visualize and evaluate this finding, we generated stage-specific aggregate footprint profiles for select TFs (Fig. 2i, Fig. S11h). Nfix, Nfic, and Nfia displayed TF activity only in $FT_{e16.5+6h}$ while Nfib displayed TF activity already in $FT_{e12.5+6h}$, which significantly increased in $FT_{e16.5+6h}$ (Fig. 2i). This aligns with the gradual increase in gene expression patterns of NFI family TFs observed in the transcriptomic data (Fig. S11i). Next, to assess whether regions where NFI family TFs binds (footprint sites) exhibit dynamic changes in accessibility, we calculated the fragment distribution within these regions. Coverage plots displayed a temporal increase in accessibility from $FT_{e12.5+6h}$ to $FT_{e16.5+6h}$ at Nfib, Nfia, Nfic and Nfix footprint sites (Fig. 2j, Fig. S11j). These results indicate a potential association of these factors with the observed chromatin dynamics, highlighting their likely role in chromatin remodelling.

Taken together, these findings demonstrate that FT^+ cohorts exhibit stage-specific chromatin accessibility, driven mainly by CREs. Furthermore, the NFI family of TFs plays a crucial role in characterizing $FT_{e16.5+6h}$ cells based on their expression, early activation of regulatory elements, and footprint.

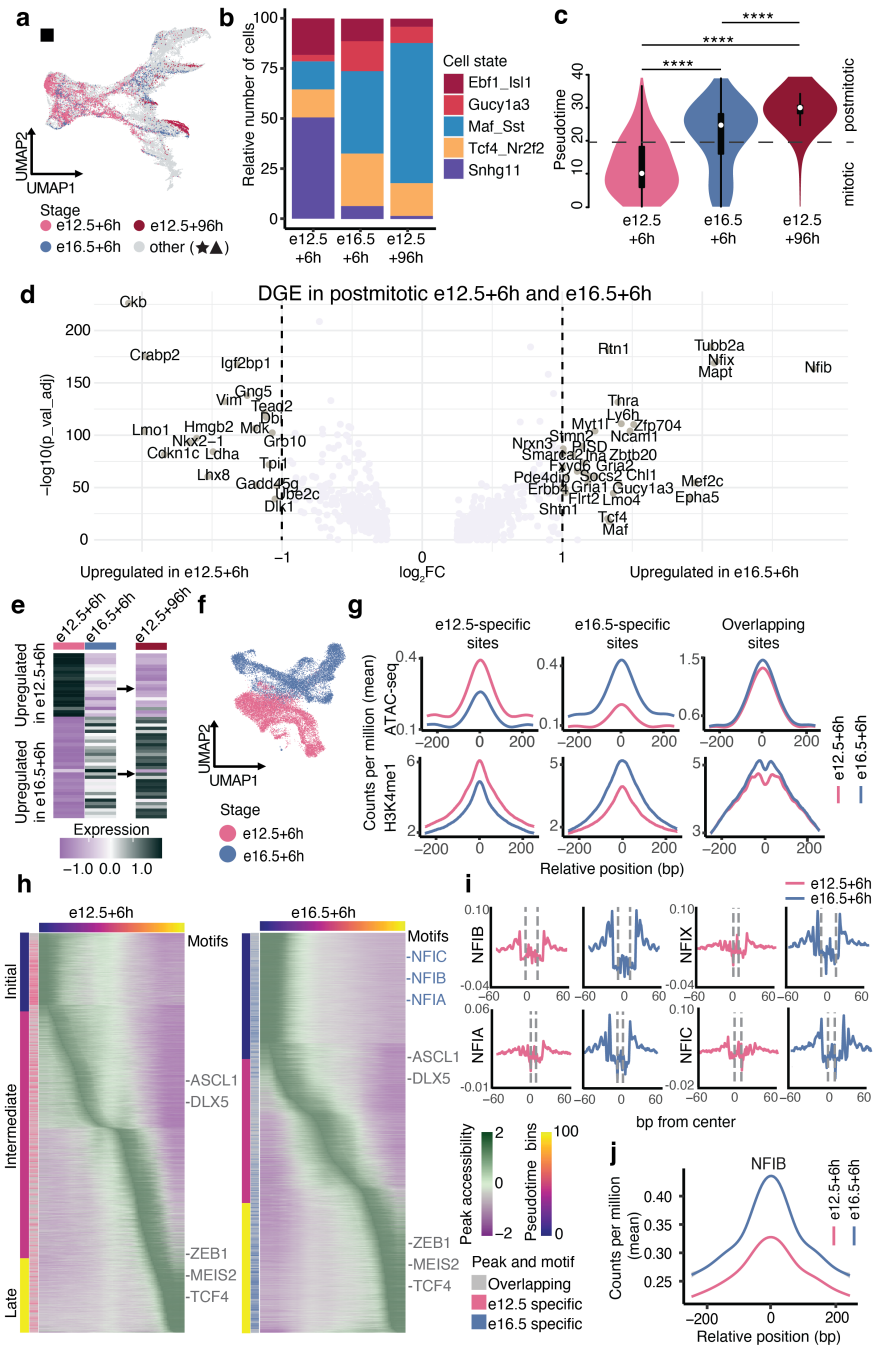

Figure 2: Timing of neurogenesis influences maturation competence. **a**, UMAP plot showing FlashTag (FT) datasets coloured by injection and collection stage; injection at e12.5 and e16.5, scRNA-seq after six hours or 96 hours. **b**, Barplot showing relative cell number of postmitotic neuronal states in $FT_{e12.5+6h}$, $FT_{e16.5+6h}$ and $FT_{e12.5+96h}$. **c**, Violin plots showing the distribution of FT^+ cells along the combined pseudotime trajectory, displayed for each condition; two-sided Wilcoxon rank sum test (****adjusted P¡0.001). The central point within the plot represents the median (50th percentile), the box represents the range between the first and third quartile (25th–75th percentile). **d**, Volcano plot displaying differential gene expression (DGE) in postmitotic cells of $FT_{e12.5+6h}$ and $FT_{e16.5+6h}$; 1¡$\log_2$FC¡−1, adjusted P¡0.05. **e**, Heatmap showing average scaled expression of differential genes in $FT_{e12.5+6h}$ and $FT_{e16.5+6h}$ postmitotic cells; visualised in all FT^+ conditions. **f**, UMAP plot showing scATAC-seq datasets; FT injection at e12.5 and e16.5, followed by scATAC-seq after 6 hours.

Figure 2:
g, Coverage plot displaying ATAC-seq and H3K4me1 signal intensity for peak categories. X-axis is relative position (base pairs) and y-axis is counts per million (mean). **h**, Heatmap displaying the accessibility of cis-regulatory elements across pseudotime for $FT_{e12.5+6h}$ and $FT_{e16.5+6h}$. Peaks are divided into "initial", "intermediate" and "late" based on accessibility profiles along pseudotime bins. Overlapping peaks are annotated in grey and unique peaks are annotated by stage-specific colours. Common motifs are coloured grey and unique motifs are coloured black. **i**, Aggregate footprint profiles of NFI family TFs in $FT_{e12.5+6h}$ and $FT_{e16.5+6h}$ **j**, Coverage plot showing chromatin accessibility dynamics at NFIB footprint sites for $FT_{e12.5+6h}$ and $FT_{e16.5+6h}$ datasets

Nfib regulates the network underlying maturation competence

When comparing scATAC-seq profiles between $FT_{e12.5+6h}$ and $FT_{e16.5+6h}$, we found distal regulatory elements (i.e. enhancers) to be the prime source of heterogeneity. To comprehensively infer enhancer-driven regulatory interactions, we used SCENIC+ (Gonzalez-Blas et al., 2023) with scRNA- and scATAC-seq data from $FT_{e12.5+6h}$ and $FT_{e16.5+6h}$. By combining information about gene expression with chromatin accessibility, we were able to link genomic binding events (i.e. a TF binding to a regulatory site) to downstream target genes. We grouped cells by collection stage (e12.5 and e16.5) and broad states (APs, BPs, and precursors), obtaining six groups in total (Fig. S12a). After running the SCENIC+ pipeline with standard filtering, the resulting GRN contained 147 TFs that bound on average 168 sites, with each site regulating one to three target genes (mean = 1.1; Fig. S12b–d). The activity of regulatory modules (i.e. expression of TF and associated target genes) was scored in each cell (Aibar et al., 2017), and enriched modules for each group were identified (Fig. S12e). Modules of canonical cell state marker genes exhibited enrichment in the respective groups: modules of Hes5, Hes1, and Pax6 in APs (Ohtsuka et al., 2001; Thakurela et al., 2016), Ascl1 and Dlx2 modules in BPs (Raposo et al., 2015; Lindtner et al., 2019), and modules of either Dlx5 or Lhx6 in neuronal precursors (Lindtner et al., 2019; Liodis et al., 2007). We also noted modules exhibiting patterns that were specific to certain cell states or developmental stages. For example, Nkx2-1 was active in BPs and precursor states, yet remained restricted to $FT_{e12.5+6h}$. In contrast, modules of NFI family TFs were active across all cell states in $FT_{e16.5+6h}$, with the highest activity in APs compared to BPs and precursor cells.

Next, we inferred active gene regulatory interactions specific to the six groups by filtering the GRN for modules active in over 50% of cells per group and applied an additional filter on downstream target genes based on gene expression level (normalized expression ¿ 0.5; methods). We obtained six subnetworks, each containing state and stage specific modules of active TFs and target genes. We compared subnetworks of APs, BPs, and precursors across stages to infer dynamic modules and the regulatory interactions between them (methods). Specifically, we focused on subnetworks of APs to identify modules that maintain or modulate progenitor competence. Modules of canonical inhibitory neuron markers like Dlx1, Dlx2, and Arx were maintained throughout all stages (Lindtner et al., 2019; Colasante et al., 2015), whereas modules linked to progenitor self-renewal, like Hmga2, Nr2f1, and Nr2f2 (Nishino et al., 2008; Bertacchi et al., 2020), were enriched in e12.5 APs (Fig. 3a). APs at e16.5 were characterized by enriched activity of Nfib, together with Nfia, Nfix, Pou3f2, Meis2, and Tcf4. In line with previous studies, Nfib acts as an upstream regulator of Nfix (Matuzelski et al., 2017), but also as an upstream regulator of Nfia, Pou3f2, Meis2, and Tcf4 (Fig. 3a). The Nfib-led regulatory cluster was consistently enriched in BPs and precursors at e16.5 (Fig. S13b,c), suggesting a role of Nfib as a master regulator.

Of particular interest to us was the interaction between Nfib with Meis2 and Tcf4, which are TFs specific to the development of inhibitory projection neurons and interneurons, respectively (Su et al., 2022; Wang et al., 2022). Moreover, these three TFs share common direct target genes in different cell states of $FT_{e16.5+6h}$ (Fig. S13d), suggesting combinatorial binding of Nfib with Tcf4 or Meis2. To test this hypothesis, we utilized TFCOMB (Bentsen et al., 2022) to analyse peaks from $FT_{e12.5+6h}$ and $FT_{e16.5+6h}$ scATAC-seq datasets (Fig. S13e). Interestingly, we observe collaboration of Nfib with these factors at both stages, with higher cosine scores and more binding events for Nfib-Tcf4 and Nfib-Meis2 in e16.5 peaks (Fig. 3b, Fig. S13e). We identified direct downstream target genes shared between Nfib, Meis2 and Tcf4 (Fig. 3c). Gene Ontology (GO) enrichment analysis of the downstream genes indicated involvement in processes related to brain development, neuron fate specification, and positive regulation of cell proliferation (Fig. S13f). Next, we identified a group of genes that were dynamic across the maturation trajectory and inferred their upstream TFs in FT^{+}

cohorts. We sorted TFs by the number of regulated maturation genes. Temporally conserved TFs like Dlx1 and Lhx2 and e16.5-specific TFs such as Nfib and Nfix (Fig. S14a–c) were regulating the largest number of genes, confirming our previous observations.

In summary, we observed a regulatory cluster characteristic of mitotic and postmitotic cells of the e16.5 cohort. This cluster is led by Nfib that regulates and interacts with Meis2 and Tcf4 via direct targeting and combinatorial binding. Additionally, Nfib was found as an upstream regulator of genes dynamic across the maturation trajectory. Together, these findings suggest that this GRN is linked to the shift in maturation competence.

Influence of extrinsic environment on maturation competence

To investigate whether the extrinsic environment affects maturation competence in APs at different stages, we performed homo- and hetero-chronic transplantation experiments and assessed the PT scores along with the expression of genes downstream of Nfib, Tcf4 and Meis2.

We injected CFSE into the ventricles of donor mouse embryos at e12.5 and e16.5. One hour later, we dissected and dissociated the GE, resulting in a cell suspension comprising FT-labelled APs, unlabelled BPs, and unlabelled precursor cells. The cell suspension was transplanted homo- and hetero-chronically into host embryos via intraventricular injection ($AP_{e12.5 \rightarrow e12.5}$/$AP_{e12.5 \rightarrow e16.5}$ and $AP_{e16.5 \rightarrow e16.5}$/$AP_{e16.5 \rightarrow e12.5}$), as described by Oberst *et al.* (Oberst et al., 2019). Forty-eight hours after transplantation, we collected the GE from the host embryos, FT^+ cells were isolated by FACS, and their transcriptome was assessed via bulk RNA sequencing (Fig. S15a,b,c). At the collection stage, cells had entered the tissue and started to migrate away from the ventricular zone (Fig. S15d).

Employing clusters of our combined scRNA-seq data as reference, we used Bisque to estimate the proportions of different neuronal states in transplantation-derived datasets (Jew et al., 2020) (Fig. S16a-c). We then assigned a score to each replicate by using the average PT score per reference cluster and weighted it according to the inferred cell state proportions. The PT scores were higher when APs were transplanted into an e16.5 environment ($AP_{e12.5 \rightarrow e16.5}$, $AP_{e16.5 \rightarrow e16.5}$)

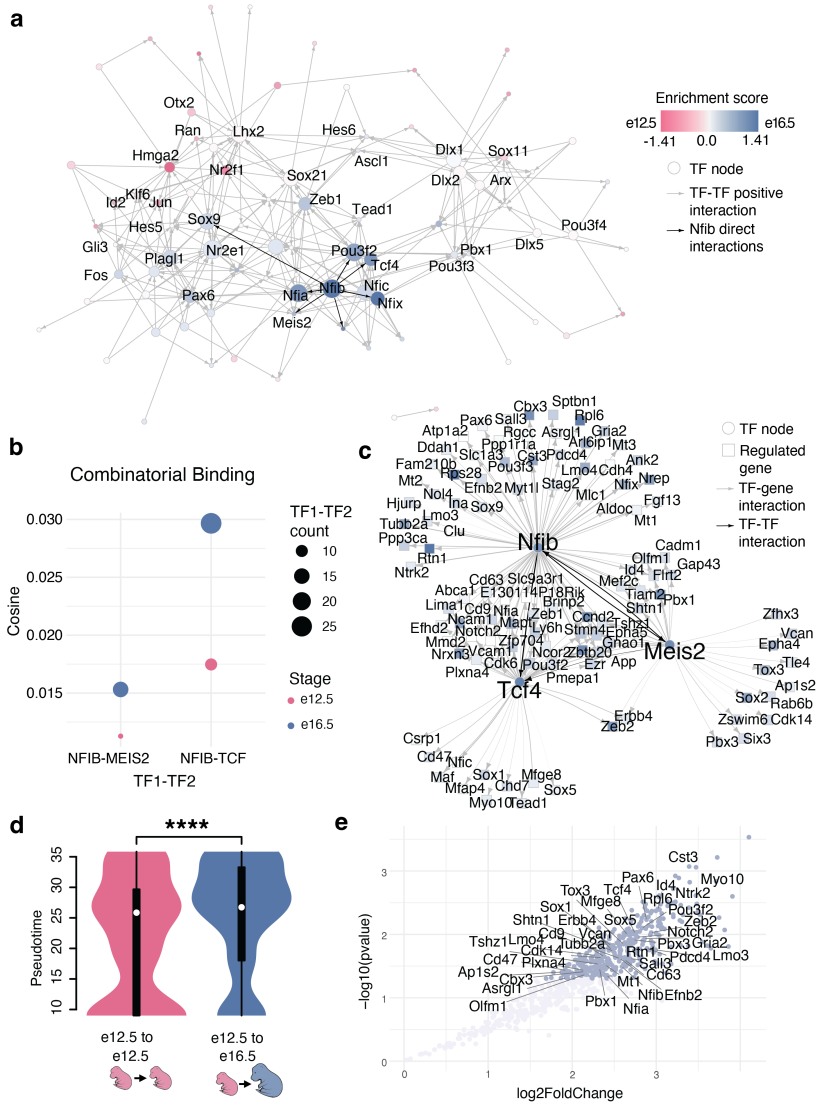

Figure 3: Nfib regulates a shift in gene-regulatory programs. **a**, GRN graph displaying interactions between TFs active in APs. Node colour indicates enrichment score by stage and node size indicates number of direct targets per TF. Select TFs are annotated. Direct interactions originating from Nfib are highlighted. **b**, Dot plot showing cosine score on the y-axis and TF pairs on the x-axis. Colour and size indicate the stage and the number of occurrences of TF1-TF2, respectively. **c**, GRN subgraph highlighting downstream targets of Nfib, Tcf4 and Meis2 at e16.5. Nfib, Tcf4 and Meis2 nodes are indicated by node shape. Interactions between Nfib, Tcf4 and Meis2 are highlighted. Node color reflects the enrichment score by stage. **d**, Distribution of transplanted cells along pseudotime in $AP_{e12.5 \rightarrow e12.5}$ and $AP_{e12.5 \rightarrow e16.5}$; two-sided Wilcoxon rank sum test (****P¡0.001). **e**, Differentially expressed genes between $AP_{e12.5 \rightarrow e12.5}$ and $AP_{e12.5 \rightarrow e16.5}$; 1¡$\log_2$FC¡−1, P¡0.05. Only genes downstream of Nfib, Meis2 and Tcf4 are labelled.

compared to an e12.5 environment ($AP_{e12.5 \rightarrow e12.5}$, $AP_{e16.5 \rightarrow e12.5}$; Fig. 3d, Fig. S16d). To identify the transcriptomic differences resulting from transplantation, we filtered the count matrix by highly variable genes from our combined datasets and used DeSeq2 (Love et al., 2014) for differential expression analysis (Fig. 3e, Fig. S16e). Notably, Nfib and many of its downstream genes (among other genes) exhibited increased expression in $AP_{e12.5 \rightarrow e16.5}$ compared to $AP_{e12.5 \rightarrow e12.5}$. However, we did not observe significantly downregulated genes (Fig. 3e). Furthermore, only two genes downstream of Nfib (Mlc1 and Aldoc) were significantly downregulated in $AP_{e16.5 \rightarrow e12.5}$ compared to $AP_{e16.5 \rightarrow e16.5}$.

These findings indicate an involvement of the extrinsic environment in shaping the maturation competence of transplanted cells. The patterns of PT and gene expression was reminiscent of the recipient stage. The gene expression change after transplantation suggests that maturation competence is likely a mechanism that operates through acquisition rather than loss of specific genes.

Discussion

Our study shows that the competence of GABAergic progenitors is dependent on the timing of neurogenesis and influences maturation – but not differentiation – of their neuronal outcome. Cell-intrinsic attributes, which include the expression of TFs, chromatin remodelling, and the re-organisation of the underlying GRN, as well as cell-extrinsic cues, all contribute to stage-specific maturation competence. The results reveal a mechanism that might adjust for differences in the time available for migration and network integration between early and late born neurons.

Our data revealed that the degree of transcriptomic maturation in late born GABAergic neurons is comparable to that of early born GABAergic neurons, which have already undergone migration and integration. The birthmark of maturation is likely conveyed from GABAergic mitotic progenitors to their daughter cells, inscribed in chromatin through priming of regulatory regions. In particular, Nfib, a component of the NFI family of transcription factors, exhibits high regulon activity in APs

349 at late stages of neurogenesis. NFI factors are known to regulate both neuronal and glial lineages
350 during central nervous system development (Bunt et al., 2017). Furthermore, they also function
351 as cofactors for FOXP2 to facilitate chromatin opening and activate neuronal maturation genes in
352 human subplate and deep layer cortical neurons (Hickey et al., 2019). In their absence, neuronal
353 progenitors in the mouse cortex and retina fail to differentiate (Betancourt et al., 2014; Harris et al.,
354 2016; Clark et al., 2019). NFI factors have been shown to regulate chromatin through various
355 mechanisms, such as binding to nucleosomes (Chávez and Beato, 1997) and chromatin modifiers
356 (Liu et al., 2001), opening chromatin (Adam et al., 2020), controlling chromatin loop boundaries,
357 and directly altering histone modifications (Pjanic et al., 2013). In our data, Nfib promotes and forms
358 partnerships with essential regulators of GABAergic IN and PN development, such as Tcf4 and
359 Meis2 (Wang et al., 2022; Su et al., 2022; Dvoretskova et al., 2023), inducing more mature neuronal
360 outcome as neurogenesis proceeds. We propose that Nfib may prime enhancer regions in APs of the
361 GE, initiating chromatin remodelling and leading to stage-specific maturation competence.

362 Other mechanisms have been proposed to govern neuronal maturation, such as the rate of
363 metabolic activity in mitochondria (Iwata et al., 2023) or selective translation of epigenetic modifiers
364 (Wu et al., 2022). Furthermore, a recent study has shown that the release of an epigenetic barrier
365 sets the timing of maturation in human neural progenitor cells, with key factors being EZH2,
366 EHMT1/2 and DOT1L (Ciceri et al., 2024). Nfib has been previously shown to repress Ezh2
367 during corticogenesis (Piper et al., 2014), suggesting a potential parallel contribution of the different
368 mechanisms to neuronal maturation.

369 The observed maturation shift in the GABAergic neuronal outcome throughout neurogenesis
370 might serve for newly born neurons to adjust for differences in the time available for migration and
371 network integration between early and late born neurons. For example, CGE-derived interneurons
372 enter the cortical plate synchronously, regardless of their birthdate (Miyoshi and Fishell, 2011).
373 However, the physiological and morphological properties assessed at a postnatal stage (P8) of striatal
374 GABAergic neurons exhibited differences between early and late born cells.

375 The maturation shift is likely tied to an interplay of extrinsic and intrinsic factors. This is

evidenced by the transplantation of GABAergic progenitor cells that adjust to their host environment through the acquisition – rather than loss – of genes. Different extrinsic influences have been shown to affect neuronal progenitors, such as the feedback from newborn cells (Reillo et al., 2017), exchange of extracellular vesicles (Pipicelli et al., 2023), and tissue stiffness (Ryu et al., 2021). Further investigation is needed to uncover the mechanisms through which GABAergic APs synchronize with the host environment.

While multiple studies described temporal and spatial differentiation patterns in GABAergic neurons (Kelly et al., 2018; Inan et al., 2012; Wonders et al., 2008; Butt et al., 2008; Flames et al., 2007; Fogarty et al., 2007; Miyoshi et al., 2007), there is little evidence of a fate birthmark transmitted from APs to their daughter cells. By contrast, glutamatergic neurons display a birthdate-dependent generation of transcriptomically distinct postmitotic cells that is linked to a progression in the differentiation competence of their progenitors (Di Bella et al., 2021; Telley et al., 2019; Vitali et al., 2018; Yoon et al., 2018). If not through a sequential mechanism, what drives diversity within the GE? Other factors, such as the mode of cell-division (Petros et al., 2015; Kelly et al., 2018), cell-cycle length (Glickstein et al., 2007; Lodato et al., 2011; Zong et al., 2022), progenitor heterogeneity (van Heusden et al., 2021), spatial subdomains, and transcription factors that transduce patterning signals (Rubenstein and Puelles, 1994; Shimamura et al., 1995; Wichterle et al., 2001; Nery et al., 2002; Xu et al., 2004; Wonders and Anderson, 2006; Flames et al., 2007; Fragkouli et al., 2009; Flandin et al., 2010; Sandberg et al., 2016; Dvoretskova et al., 2023) have been shown to underlay the generation of diverse GABAergic types.

This study contributes to the broader discourse on neuronal maturation, offering insights into the plasticity and commitment of GABAergic progenitors.

Supplementary Figures

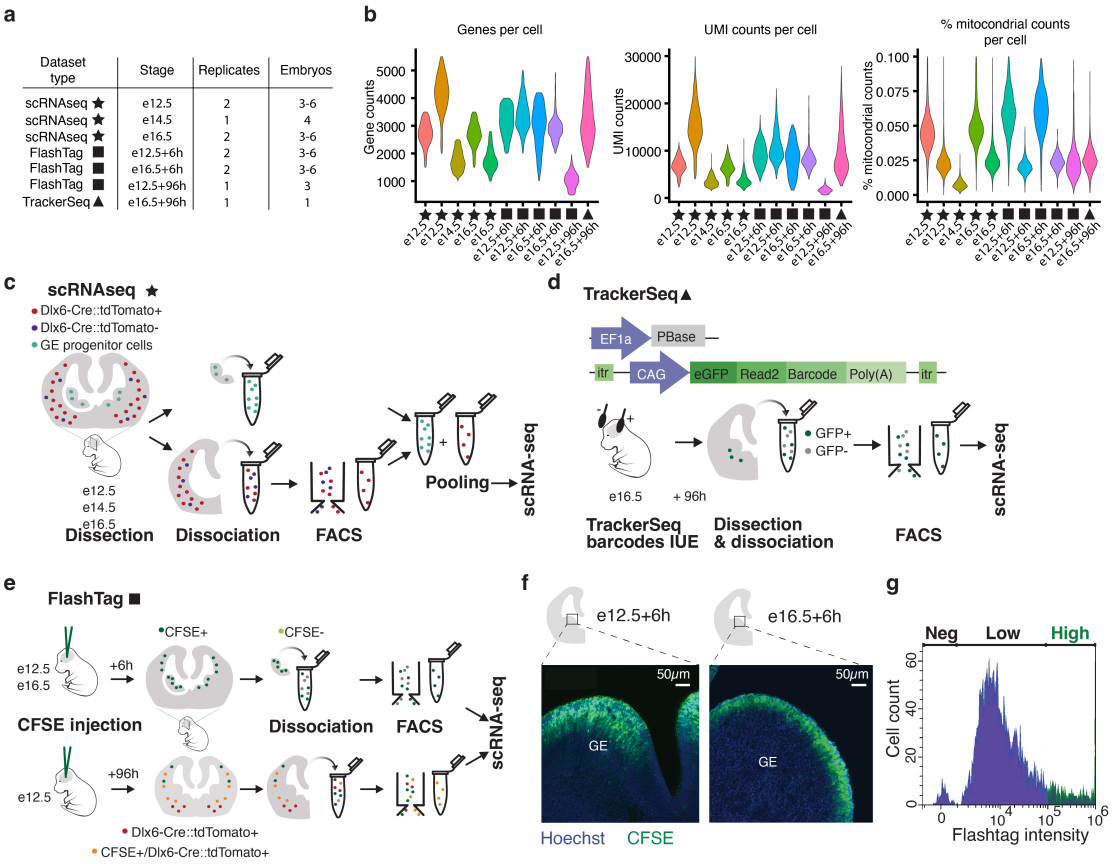

Supplementary Figure 1: Overview of the experimental workflow and dataset information. **a**, Table with dataset type, collection stage, number of replicates, and number of collected embryos. **b**, Violin plot illustrating the number of genes, counts and mitochondrial gene fraction per cell for each replicate. **c**, Schematic representation of the experimental procedure to generate the scRNAseq datasets. **d**, Schematic representation of the experimental procedure to generate the TrackerSeq datasets. **e**, Schematic representation of the experimental procedure to generate FlashTag datasets. **f**, FT^+ cells, injected with CFSE. Injection at e12.5 and e16.5, collection after six hours; coronal sections of ganglionic eminences (GE). **g**, FACS of high-intensity FT^+ cells for FlashTag dataset processing.

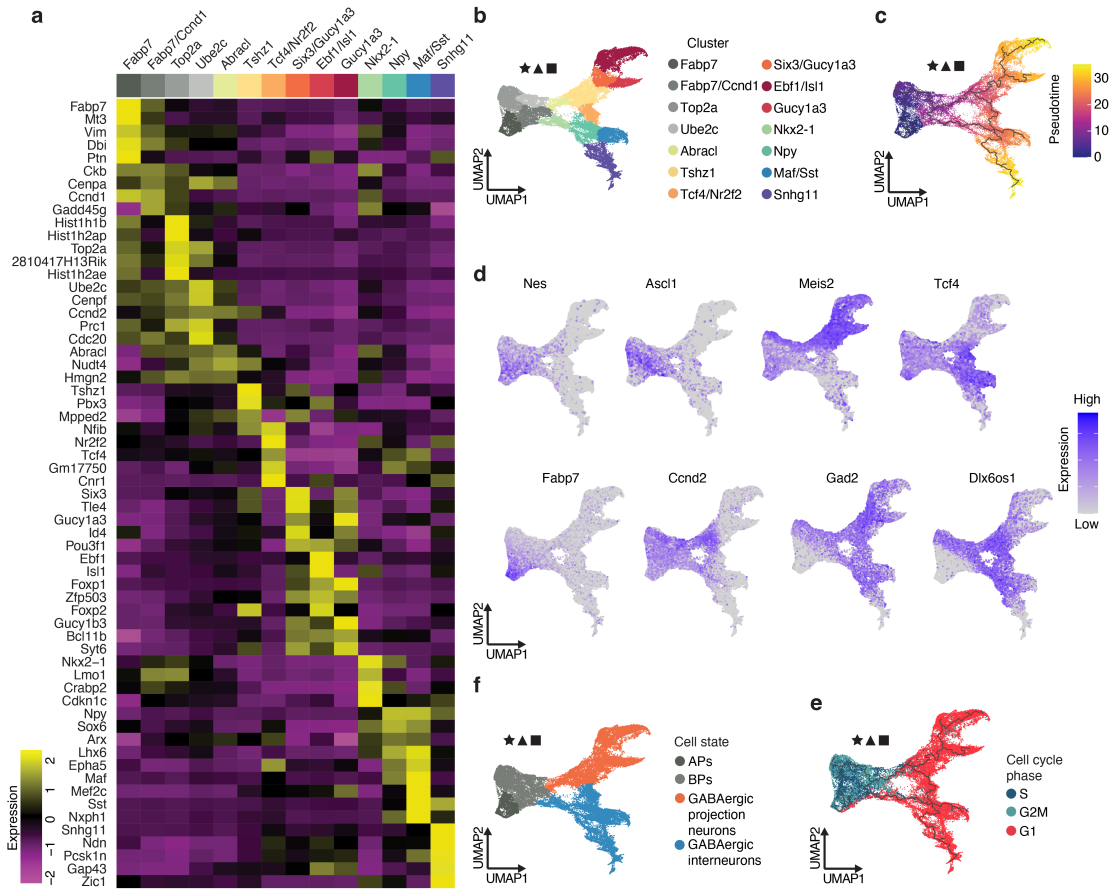

Supplementary Figure 2: Cell type characterization in the GABAergic lineage. **a**, Heatmap of top five differentially expressed genes in GABAergic cell clusters. **b**, UMAP plot of combined datasets with cells coloured by cluster identity. Clusters are annotated by one or two top marker genes. **c**, UMAP plot of combined datasets with inferred Monocle3 trajectory. Cells are coloured by pseudotime. **d**, Expression of marker genes in the combined dataset. Nes and Fabp7 label APs, Ascl1 and Ccnd2 are markers for BPs. Post-mitotic inhibitory neurons express Gad2 and Dlx6os1. Meis2 labels PNs and Tcf4 labels INs. **e**, UMAP plot of combined datasets, with cells coloured by broad cell states. **f**, UMAP plot of combined datasets coloured by cell cycle phases.

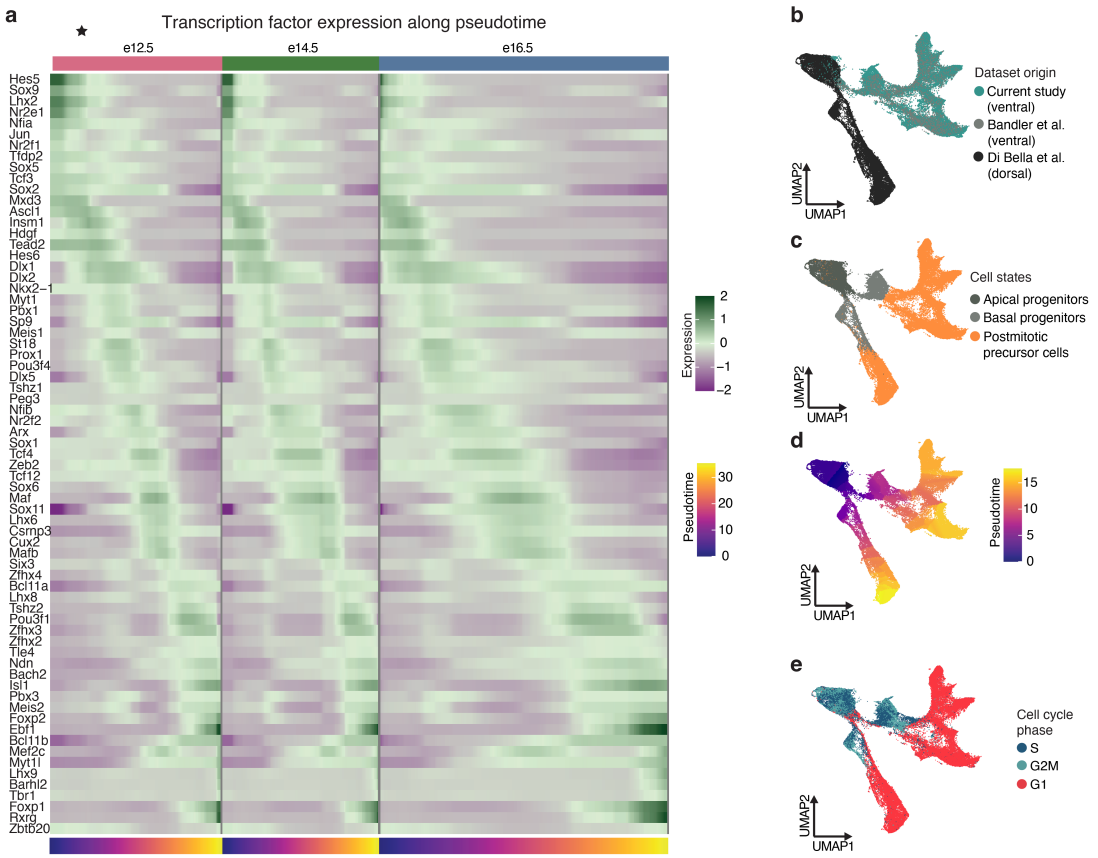

Supplementary Figure 3: Developmental dynamics in ventral and dorsal lineages. **a**, Scaled and smoothed expression of dynamic TFs in GABAergic cells. TFs are ordered by their maximum expression along the pseudotime trajectory. **b**, UMAP plot of ventral and dorsal lineage datasets from different publications. **c-e**, UMAP plot of ventral and dorsal lineage datasets, with cells coloured by broad cell state (**c**), pseudotime (**d**) and cell cycle phase (**e**).

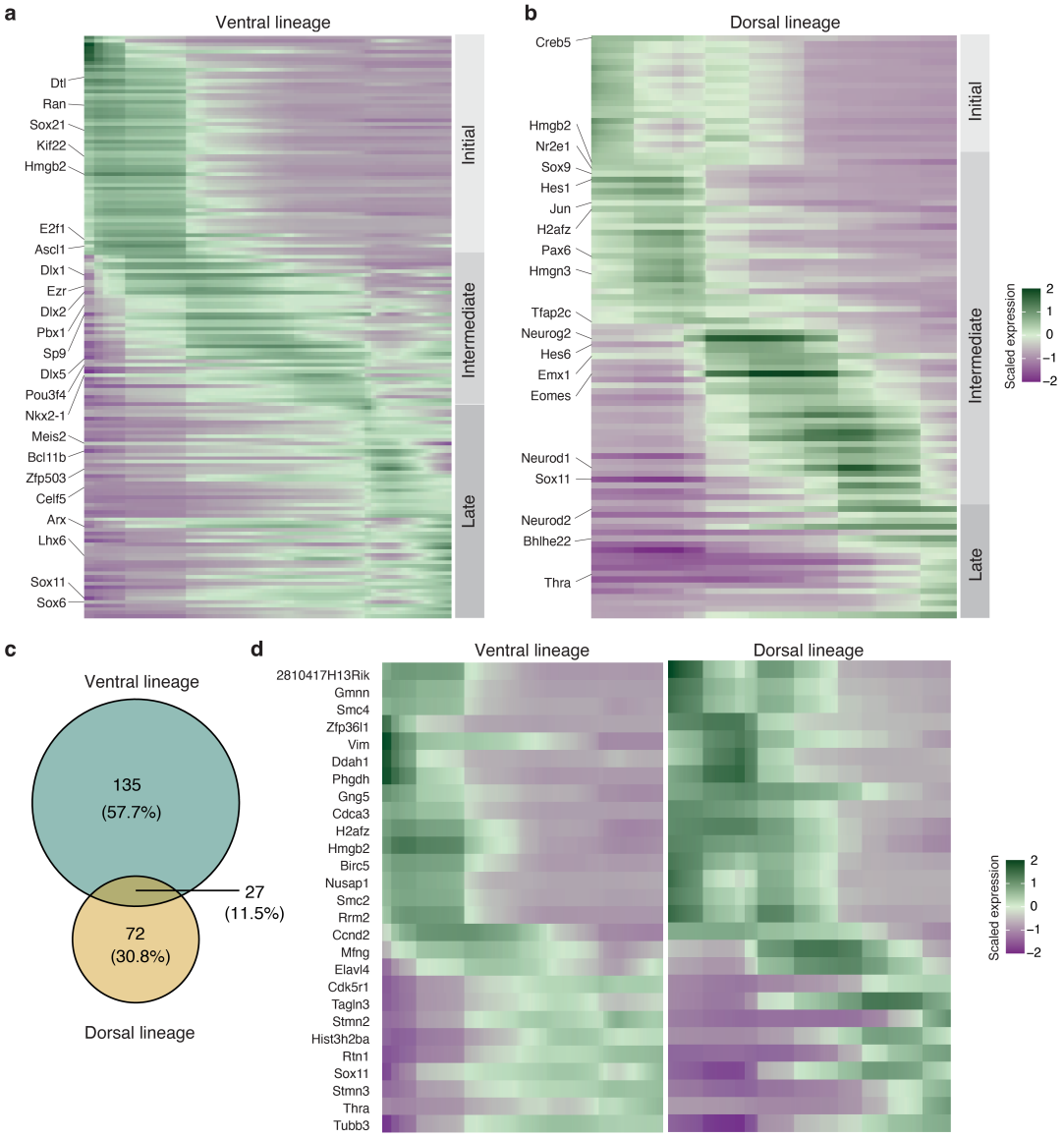

Supplementary Figure 4: Dynamic genes in ventral and dorsal lineages. **a**, Scaled and smoothed expression of genes dynamic along the maturation trajectory in ventral lineage. **b**, Scaled and smoothed expression of genes dynamic along the maturation trajectory in dorsal lineage. **c**, Number of shared and distinct dynamic genes between ventral and dorsal lineages. **d**, Expression of common dynamic genes in dorsal and ventral lineages.

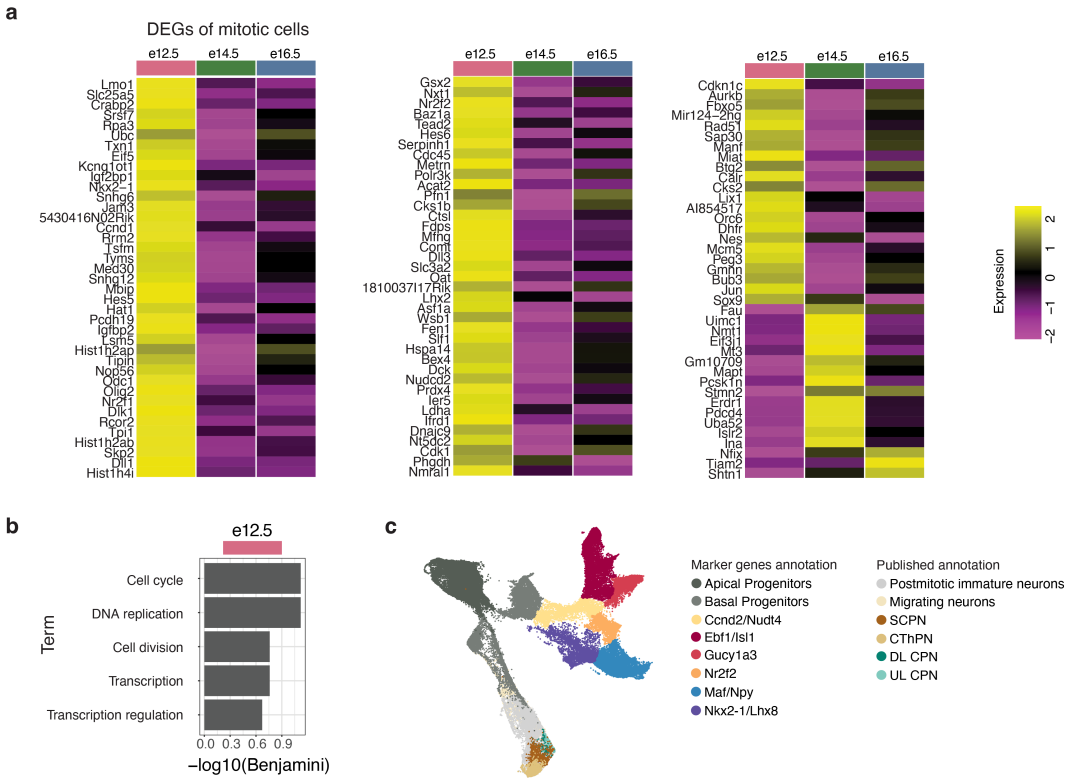

Supplementary Figure 5: Genes characterizing GABAergic mitotic progenitors at different stages. a, Average gene expression heatmap of differentially expressed genes in mitotic progenitors at e12.5, e14.5, and e16.5 in the scRNAseq dataset. **b**, Functional annotation of differentially expressed genes in e12.5 APs. Top five GO terms ranked by Benjamini-Hochberg corrected *P* values (DAVID). **c**, UMAP plot of ventral and dorsal lineages. The dorsal lineage is annotated according to Di Bella *et al.* (Di Bella et al., 2021). The ventral lineage is annotated based on top marker gene expression.

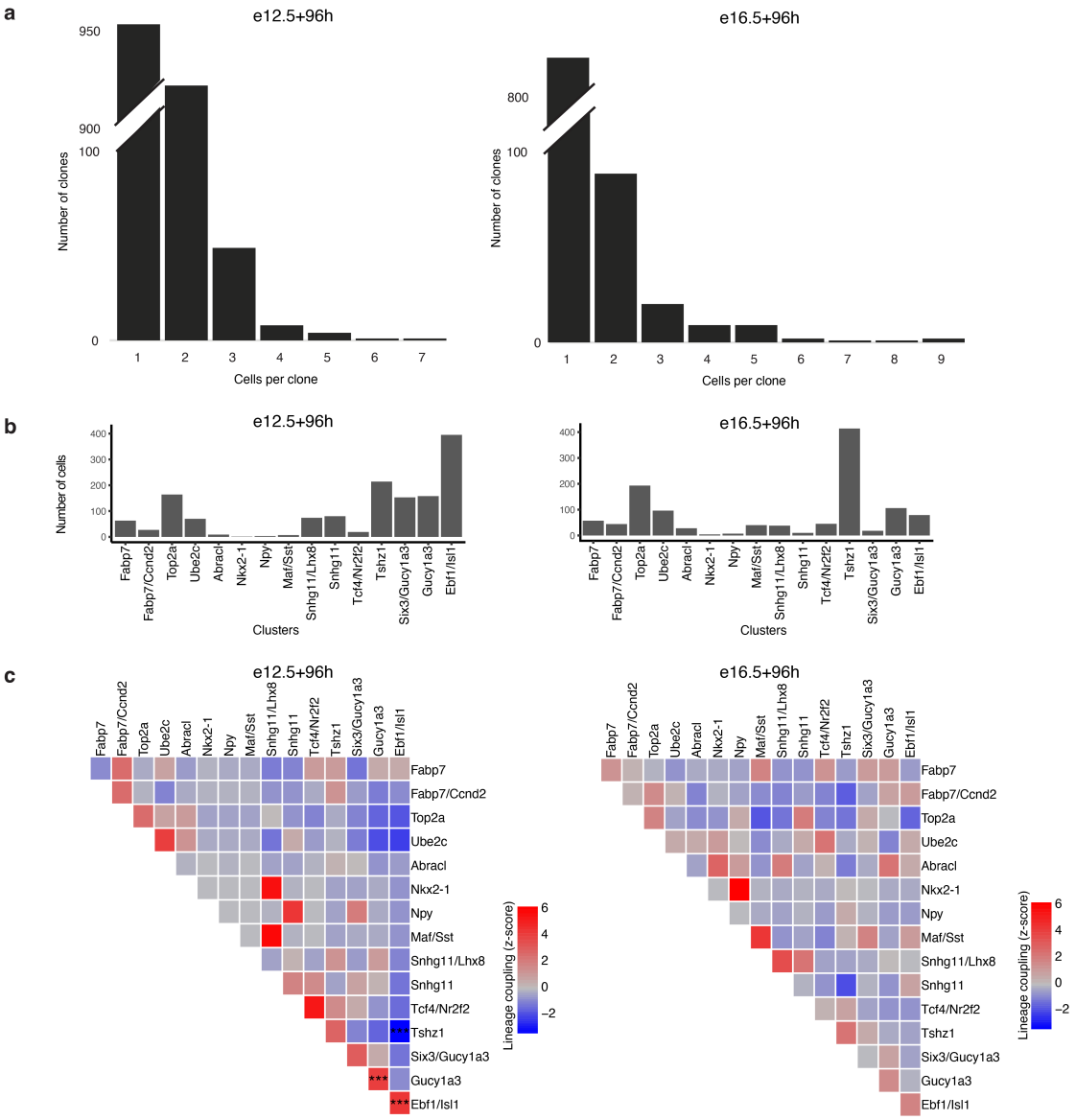

Supplementary Figure 6: Clonal distribution and coupling in TrackerSeq datasets. a, Clonal distribution in the TrackerSeq$_{e12.5+96h}$ dataset (left) and TrackerSeq$_{e16.5+96h}$ dataset (right). **b**, Barplots showing the number of cells containing clonal information per cluster in e12.5 (left) and e16.5 (right). **c**, Clonal coupling between cell states in TrackerSeq$_{e12.5+96h}$ (left) and TrackerSeq$_{e12.5+96h}$ (right). Z-scores indicate clonal coupling, with positively coupled pairs of cell states having positive z-scores and anticoupled pairs of cell states having negative z-scores. Empirical P values were calculated for each comparison and FDR-corrected (***P¡0.001).

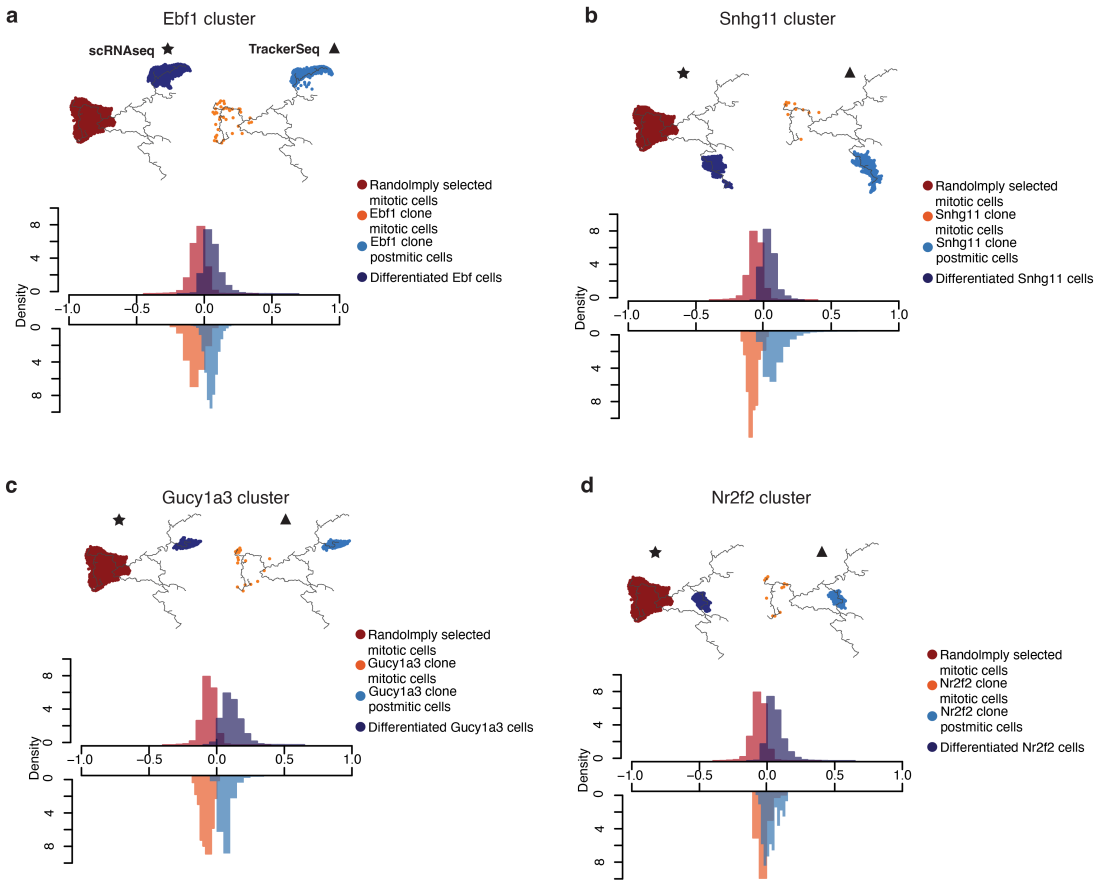

Supplementary Figure 7: Analysis of TrackerSeq-labelled clones. a-d, Correlation analysis of "non-dispersing" TrackerSeq-labelled clones. Pearson correlation coefficient calculated between cell pairs within mitotic and postmitotic clone subsets, and reference subsets. **a**, Postmitotic clones of the Ebf1 cluster, mitotic clones of the Ebf1 cluster, and randomly selected mitotic cells, correlated to the Ebf1 postmitotic reference group. **b**, Postmitotic clones of the Snhg11 cluster, mitotic clones of the Snhg11 cluster, and randomly selected mitotic cells, correlated to the Snhg11 postmitotic reference group. **c**, Postmitotic clones of the Gucy1a3 cluster, mitotic clones of the Gucy1a3 cluster, and randomly selected mitotic cells, correlated to the Gucy1a3 postmitotic reference group. **d**, Postmitotic clones of the Nr2f2 cluster, mitotic clones of the Nr2f2 cluster, and randomly selected mitotic cells, correlated to the Nr2f2 postmitotic reference group.

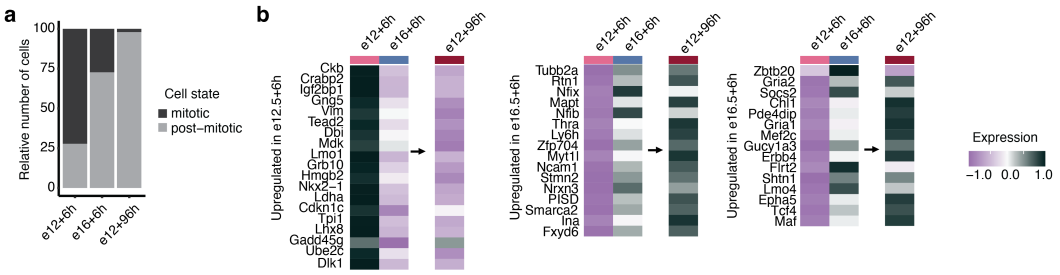

Supplementary Figure 8: Transcriptome analysis of FlashTag-labelled cohorts.
a, Barplot showing the cell ratio in different cell-cycle states for the $FT_{e12.5+6h}$, $FT_{e16.5+6h}$, and $FT_{e12.5+96h}$ datasets. **b**, Detailed heatmap of differentially expressed genes between $FT_{e12.5+6h}$ and $FT_{e16.5+6h}$; 1¡$\log_2$FC¡−1, adjusted P¡0.05. Expression is visualized in $FT_{e12.5+6h}$, $FT_{e16.5+6h}$ and $FT_{e12.5+96h}$ datasets.

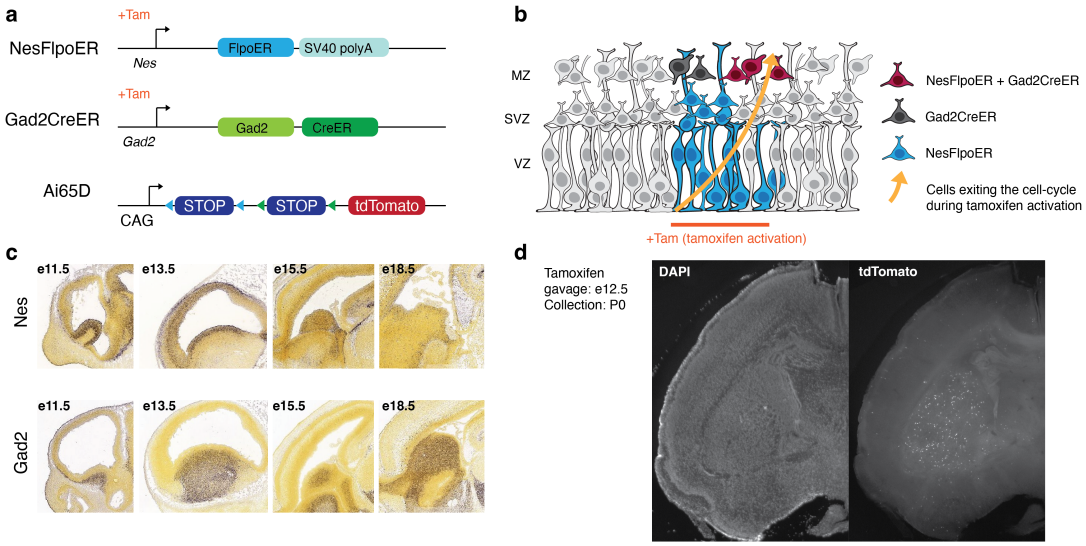

Supplementary Figure 9: An intersectional approach for GABAergic neuron birthdating.
a, Schematic illustrating the crossing of alleles: NesFlpoER allele, Gad2CreER allele, and Ai65D intersectional reporter allele. **b**, Schematic illustrating the rationale behind the birthdating method: administration of tamoxifen inducing the expression of tdTomato in a cohort of cells that was transitioning from a mitotic (Nes^+) to a postmitotic ($Gad2^+$) cell state. **c**, *In situ* hybridization images from the Allen Brain Atlas; sagittal sections. **d**, Coronal sections of brains with $DAPI^+$ (right) and $tdTomato^+$ (left) cells; tamoxifen gavage at e12.5, collection at P0.

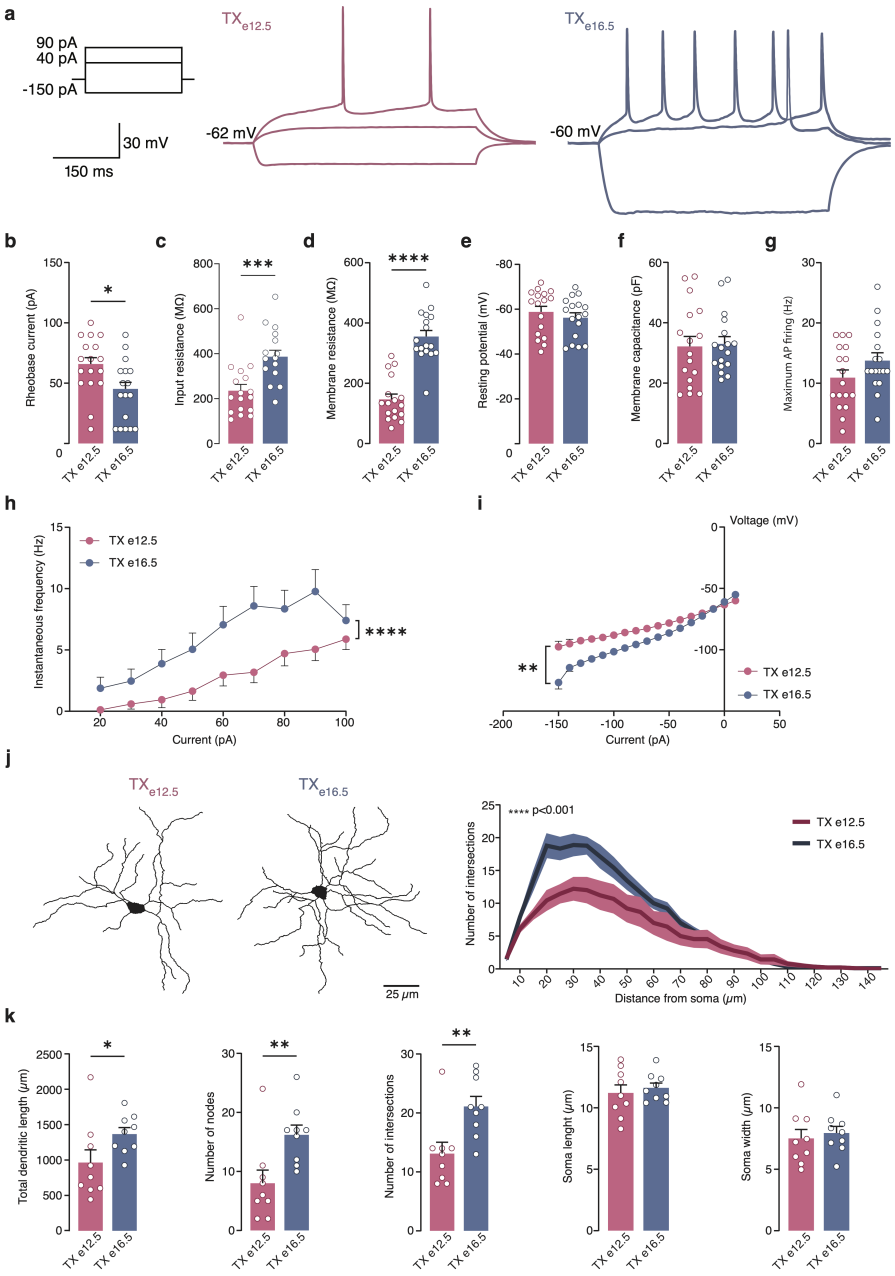

Supplementary Figure 10: Electrophysiological and morphological characterisation of $TX_{e12.5}$ and $TX_{e16.5}$ cohorts.

a, Representative voltage responses to hyperpolarising (–150 pA) and depolarising (40 and 90 pA) current pulses in $TX_{e12.5}$ and $TX_{e16.5}$ GABAergic neurons. **b–d**, Summary bar graphs of rheobase current (b), input resistance (c) and membrane resistance (d) in $TX_{e12.5}$ and $TX_{e16.5}$ GABAergic neurons. **e–g**, Summary bar graphs of resting potential (e), membrane capacitance (f) and maximum action potential (AP) firing (g) in $TX_{e12.5}$ and $TX_{e16.5}$ GABAergic neurons. **h**, Action potential firing frequency (Hz) plotted as a function of injected current steps (I-F curve). **i**, Current-voltage (I-V) plots recorded from $TX_{e12.5}$ and $TX_{e16.5}$ GABAergic neurons. **j**, Sholl analysis of reconstructed biocytin-filled GABAergic neurons recorded in the dorsal striatum region. Representative images of $TX_{e12.5}$ and $TX_{e16.5}$ neurons are shown on the left. The right panel shows the number of dendritic branches (arbor complexity) plotted against distance from the cell body (soma).

Supplementary Figure 10:
k, (From left to right) Summary of the total dendritic length, number of nodes, maximum number of intersections, soma length and soma width in $TX_{e12.5}$ and $TX_{e16.5}$ neurons. Plots represent mean ± s.e.m. and raw data points. Mann–Whitney test for all panels except for panels h,i and j (Two-way ANOVA with multiple comparisons). *P¡0.05, **P¡0.01, *** P¡0.001, ****P¡0.0001.

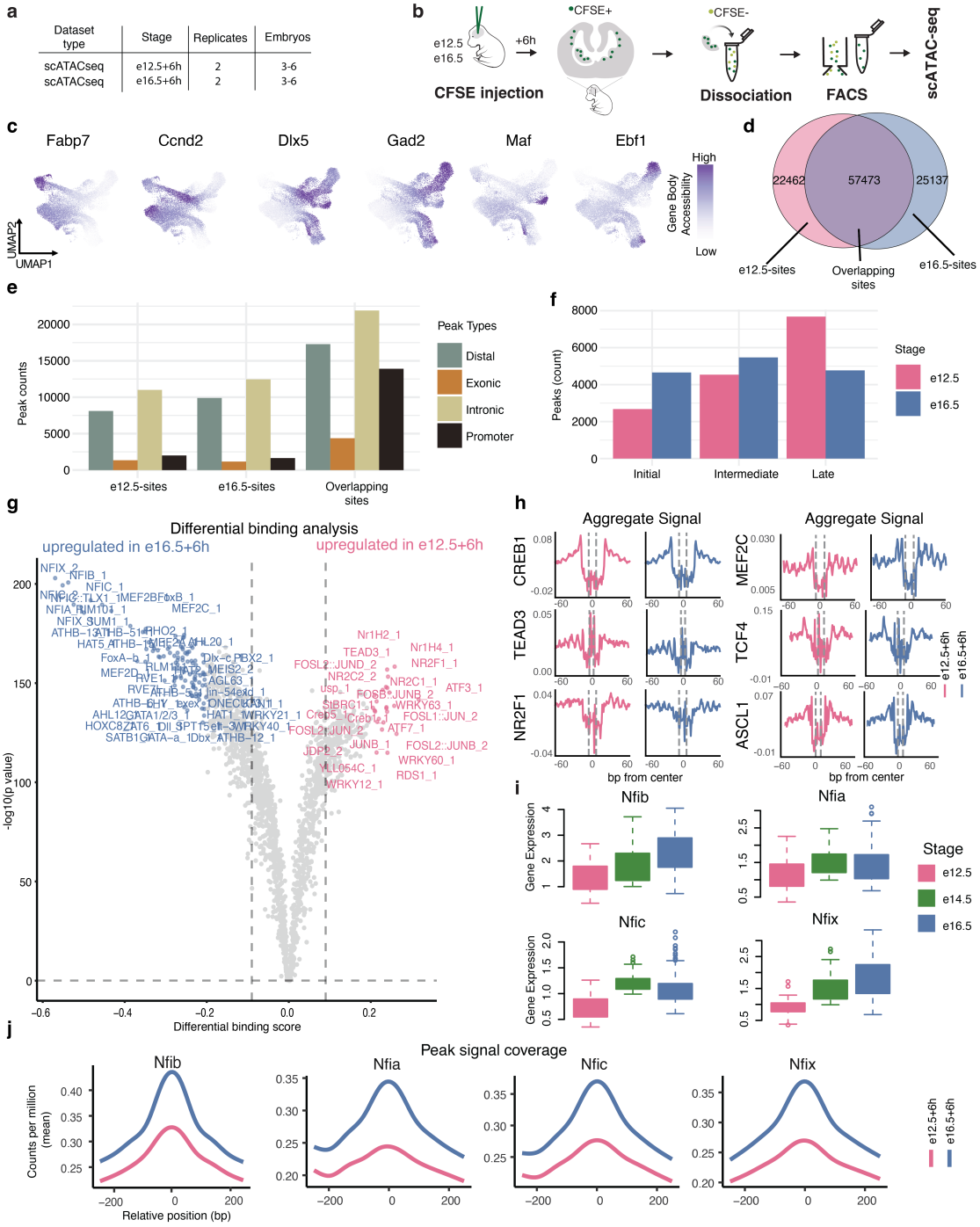

Supplementary Figure 11: Transcription factor activity and chromatin remodelling in early and late cohorts.

a, Overview of FT$^+$ scATAC-seq datasets: collection stage, number of replicates, and number of embryos. **b**, Schematic representation of the experimental procedure to generate FT$^+$ scATAC-seq datasets. **c**, UMAP depiction of gene body accessibility for marker genes. Fabp7 for APs, Ccnd2 for BPs, Dlx5 and Gad2 for postmitotic inhibitory neurons, Maf for INs and Ebf1 for PNs. **d**, Venn diagram showing the three categories of sites (e12.5 sites, e16.5 sites and overlapping sites) and the number of non-overlapping and overlapping sites. **e**, Barplot quantifying peak types (distal, exonic, intronic, and promoter) at e12.5, e16.5, and overlapping sites.

Supplementary Figure 11:
f, Barplot quantifying peak distribution across initial, intermediate, and late phases of pseudotime.**g.** Volcano plot displaying –log10(*P* value)(x-axis) and differential binding score (y-axis) of significant transcription factors. Each dot represents a motif. **h**, Aggregate footprint profiles of select transcription factors in $FT_{e12.5 + 6h}$ and $FT_{e16.5 + 6h}$. **i**, Boxplot showing normalised gene expression levels at e12.5, e14.5 and e16.5; scRNA-seq dataset. Cells with no expression of the selected genes are not displayed. **j**, Coverage plot showing chromatin accessibility dynamics at Nfib, Nfia, Nfic and Nfix footprint sites in $FT_{e12.5 + 6h}$ and $FT_{e16.5 + 6h}$ datasets.

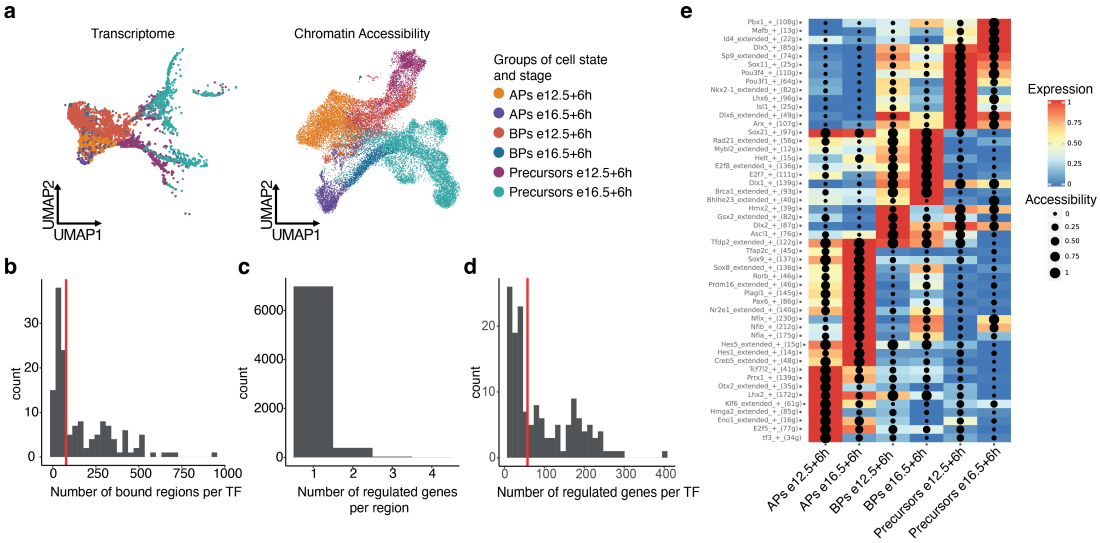

Supplementary Figure 12: Gene regulatory network of $FT_{e12.5+6h}$ and $FT_{e16.5+6h}$.
a, UMAP embedding of cells from scRNA-seq (left) and scATAC-seq (right). Cells are annotated based on broad cell state and stage. **b-d**, Distribution of the number of bound regions per TF (**b**), regulated genes per region (**c**), and target genes per TF (**d**). Red horizontal lines in (**b**) and (**d**) indicate the median of the corresponding distribution. **e**, Heatmap displaying active marker modules for stage-specific cell states. Colour indicates the scaled average expression of the module (i.e. TF expression and target genes expression). Dot size indicates scaled accessibility of associated regulatory regions. Modules are named after the TF, type of regulation (here only positive) and number of target genes.

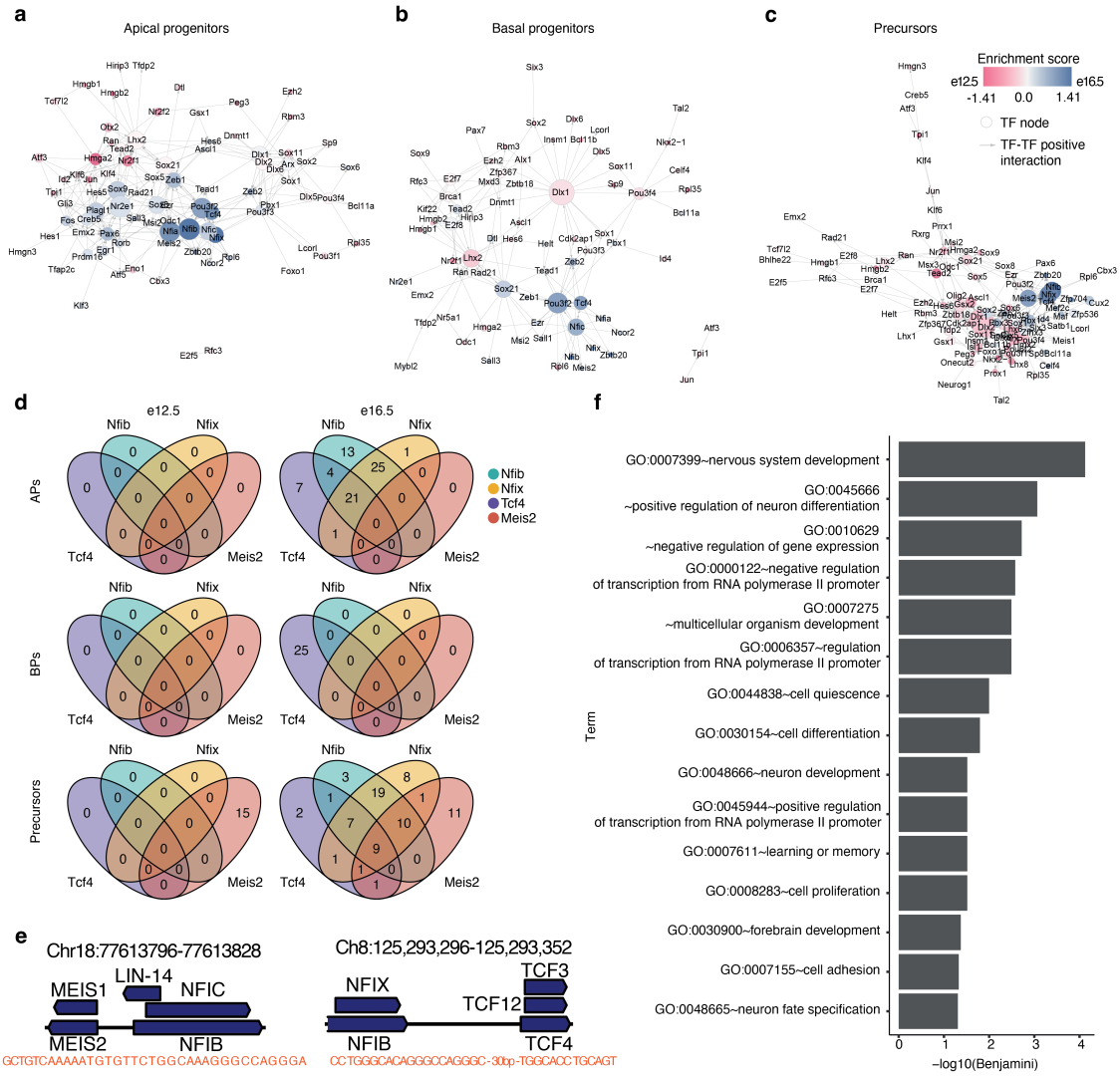

Supplementary Figure 13: Transcription factor interaction analysis in subnetworks.
a-c, Subnetwork for APs (**a**), BPs (**b**) and precursors (**c**). Each subnetwork is merged across e12.5 and e16.5, with node colour indicating the difference in expression between stages. The size of nodes reflects the number of downstream targets per TF. Subnetworks show only interaction between TFs. **d**, Number of shared and distinct regulated target genes of Nfib, Nfix, Tcf4 and Meis2 across cell states and stages. **e**, Genomic view of transcription factor binding sites for Nfib-Meis2 and Nfib-Tcf4. **f**, Significantly enriched GO-terms (Benjamini-Hochberg corrected P¡ 0.05) for target genes of Nfib and Nfix and/or Tcf4 in e16.5 cells.

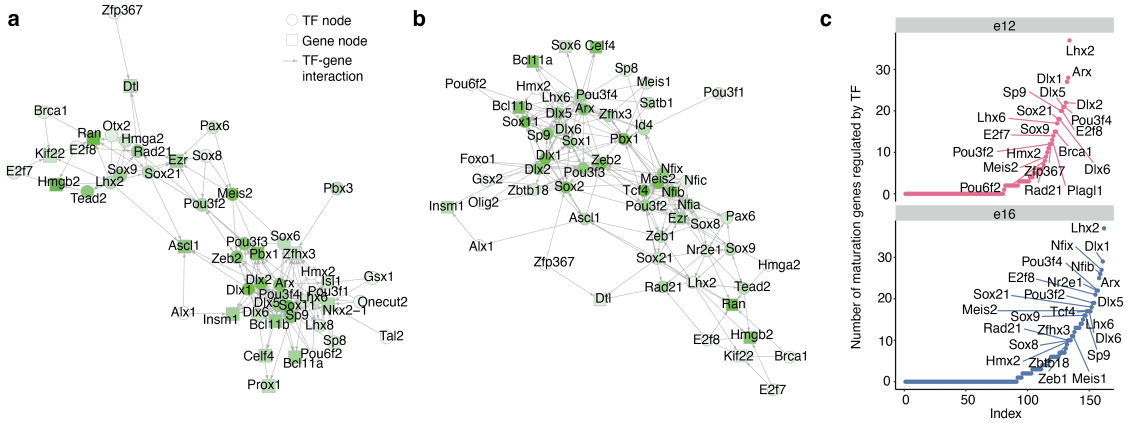

Supplementary Figure 14: Transcription factors upstream of genes dynamic along the maturation trajectory.
a, TF interaction network of TFs that regulate genes dynamic along the maturation trajectory in e12.5. Nodes are coloured by their average expression at e12.5. **b**, TF interaction network of TFs that regulate genes dynamic along the maturation trajectory in e16.5. Nodes are coloured by their average expression at e16.5. **c**, Number of bound genes per TF (out-degree) at e12.5 and e16.5; subsetted for genes dynamic along the maturation trajectory and their upstream TFs. TFs with an out-degree higher or equal than eight are labelled.

a

Donor stage	Host stage	Collection stage	Replicates	Embryos
e12.5	e12.5	e14.5	5	2-3
e12.5	e16.5	e18.5	5	2-3
e16.5	e16.5	e18.5	4	2-3
e16.5	e12.5	e14.5	4	2-3

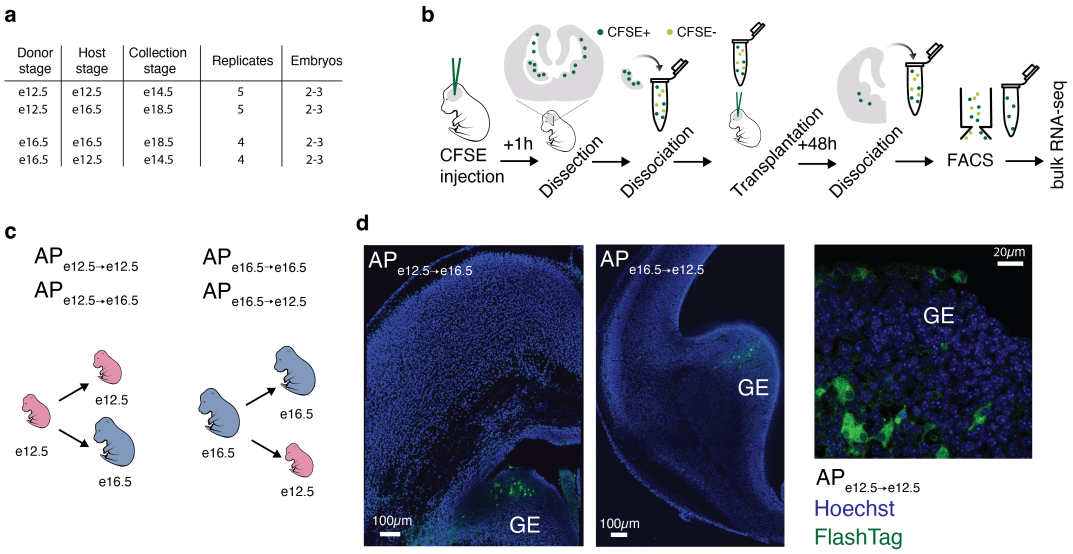

Supplementary Figure 15: Experimental overview of homo- and hetero-chronic transplantation datasets.

a, Overview table of homo- and hetero-chronic transplantation experiment datasets: donor, host, and collection stages, number of replicates and number of embryos for each condition. **b**, Schematic representation of the experimental procedure of APs labelling and homo- and hetero-chronic transplantation. **c**, Schematic overview of donor and host stages for homo- and hetero-choronic transplantation experiment. **d**, Images of coronal brain sections after FT^+ APs transplantation. APs labelled with CFSE; GE, ganglionic eminence.

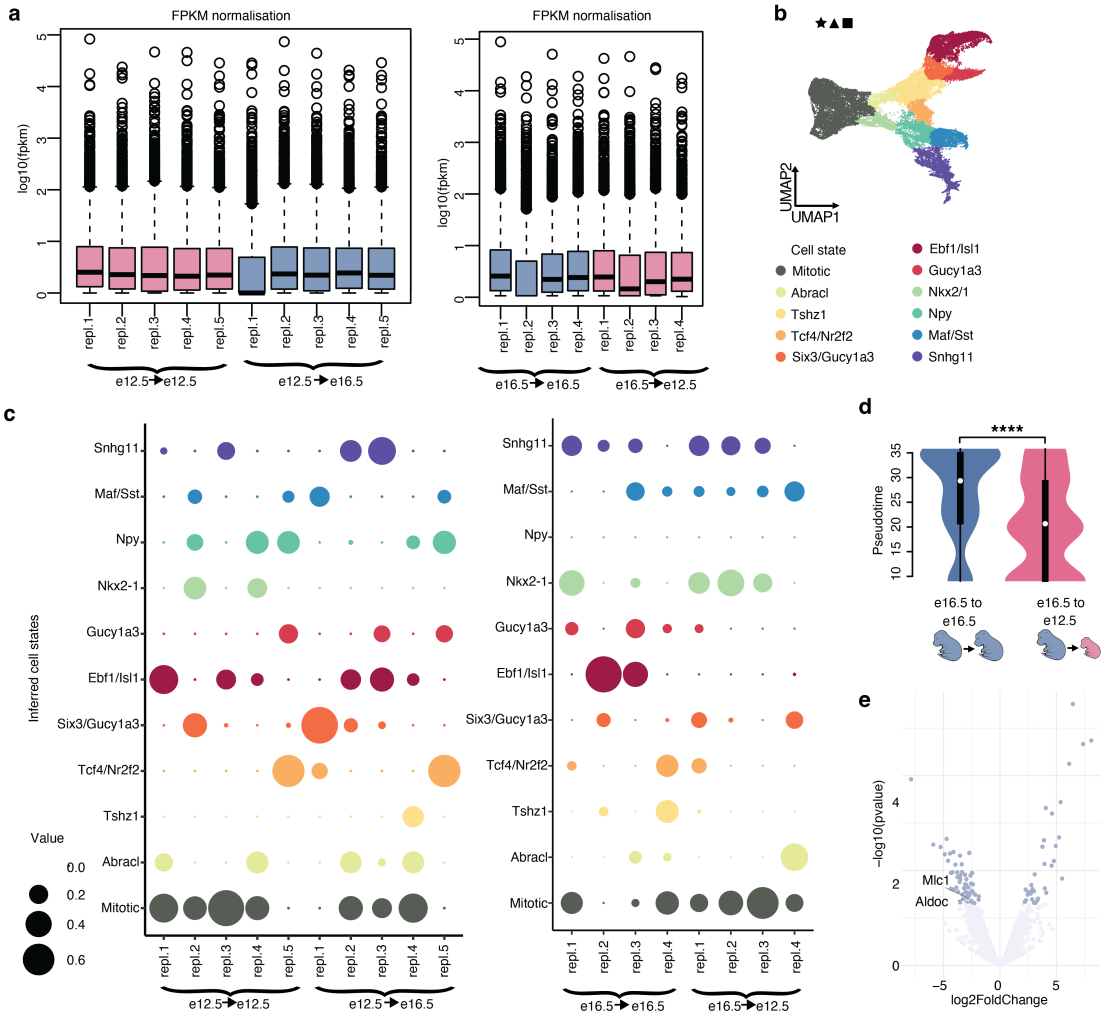

Supplementary Figure 16: Normalisation and inference of cell state composition in transplanted datasets.

a, Fpkm normalization of count matrices from bulk RNA sequencing. **b**, UMAP plot of the combined dataset utilised for cluster reference. **c**, Predicted cell state composition in each replicate. **d**, Distribution of transplanted cells along pseudotime in $AP_{e16.5 \rightarrow e16.5}$ and $AP_{e16.5 \rightarrow e12.5}$; two-sided Wilcoxon rank sum test (****adjusted P¡0.001). **e**, Differentially expressed genes between $AP_{e16.5 \rightarrow e16.5}$ and $AP_{e16.5 \rightarrow e12.5}$; 1¡$\log_2$FC¡−1, P¡0.05. Only genes downstream of Nfib, Meis2 and Tcf4 are labelled.

Tables

Gene symbol	log_2FC	Function during neurogenesis	Reference (PMID)
Tubb2a	2,06	Microtubule protein involved in neuronal migration and proliferation; mutation linked to brain malformation and epilepsy.	24702957
Rtn1	1,33	Reticulon protein localized in ER and neuronal dendrites, regulates ER activity and cytosolic calcium dynamics.	23454728, 23559015
Nfix	2,10	Transcription factor essential for normal brain development, regulates progenitor cell differentiation in the hippocampus.	23042739, 18477394
Mapt	2,08	Microtubule-associated protein with role in brain development and neurogenesis as well as detrimental role in neurodegeneration at later age.	29202785
Nfib	2,79	Transcription factor involved in neuronal radial glia differentiation and cortical development regulation.	23749646, 32166136
Thra	1,40	Nuclear hormone receptor required for normal neural progenitor cell proliferation in human cerebral cortical development.	31628250
Ly6h	1,42	Endogenous neurotoxin-like protein, inhibits alpha7 nicotinic acetylcholine receptor currents at the plasma membrane.	25716842, 32686737
Zfp704	1,51	C2H2 zinc finger protein expressed in several NC-derived lineages.	17693064
Myt1l	1,23	CCHC zinc finger TF involved in neuronal identity and maturation.	21617644, 34614421
Ncam1	1,48	Neural cell adhesion molecule important for neuronal migration, neurite developent, synaptogenesis and neural stem cells regulation.	19788570, 20038681, 17682066
Stmn2	1,14	Microtubule regulator, necessary for normal axonal outgrowth , regeneration and protection.	30643292
Nrxn3	1,01	Presynaptic transmembrane protein with role in synapse development and function.	34879268, 2847265
PISD	1,01	Mitocondrial-localized enzyme, associated with impaired mitochondrial protein homeostasis.	30858161
Smarca2	1,08	Subunit of chromatin remodelling complexes, involved in neural progenitor differentiation.	31375262
Ina	1,16	Neuronal intermediate filament protein that influence morphology and physiology of axonx.	11739575
Fxyd6	1,00	Transmembrane protein involved in Na/K pump function modulation.	33231612
Zbtb20	1,11	Transcription factor with role in neurogenesis and astrocytogenesis modulation.	27282384, 27000654
Gria2	1,15	Subunit of AMPA receptor, LOF leads to neurodevelopmental disorders.	31300657
Socs2	1,19	Intracellular protein that regulates neuron embryonic development and the neurotrophin signaling.	12368809, 24860421
Chl1	1,24	Neural recognition molecule that begatively regulates neuronal proliferation and differentiation.	20933598
Pde4dip	1,03	Protein anchoring components of the cAMP-dependent pathway in the ER to Golgi trafficking.	35346821
Gria1	1,18	Subunit of AMPA receptor, LOF leads to neurodevelopmental disorders.	35675825
Mef2c	1,95	Transcripton factor involved in interneurons fate and maturation and is linked to various neuropsychiatric and neurodevelopmental disorders.	27779093, 18579729, 32452758
Gucy1a3	1,41	Subunit of guanylate cyclase enzyme regulating MGE neurons migration and marker of indirect striatal medium spiny neurons.	24155296, 36081908
Erbb4	1,00	Receptor tyrosine kinase required for interneuron migration and inhibitory synapse formation.	15473965, 34226493
Flrt2	1,02	cell adhesion molecules with role in Tangential Migratory Streams of Cortical Interneurons.	34301831
Shtn1	1,02	Protein coding gene involved in neuronal polarization and axonogenesis.	17030985, 30733148
Lmo4	1,36	Transcriptional regulator essential for normal patterns of proliferation ans survival of neuroepithelial cells.	15691703
Epha5	1,91	Ephrin receptor protein, involved in axon guidance and synaptogenesis during development.	19326470, 20824214
Tcf4	1,32	Transcription factor regulating cortical interneuron neurogenesis.	35965434
Maf	1,34	Transcription factor regulating cortical interneuorn fate and maturation.	30699346, 32452758

Table 1: Functional summary of e16.5 enriched genes differentially expressed between $FT_{e12.5+6h}$ and $FT_{e16.5+6h}$.

Methods

Animals

All experiments were conducted according to institutional guidelines of the Max Planck Society and the regulations of the local government ethical committee (Beratende Ethikkommission nach §15 Tierschutzgesetz, Regierung von Oberbayern). All mouse colonies were maintained in accordance with protocols approved by the Bavarian government. Mice were group housed in isolated ventilated cages (room temperature $22 \pm 1°$C, relative humidity $55 \pm 5\%$) under a 12 h dark/light cycle with ad libitum access to food and water. Mouse strains used are the following: wild type C57BL/6NRj, Tg(dlx6a-cre)1Mekk (Dlx6-Cre; JAX:008199) (Monory et al., 2006), Rosa26LSL-tdTomato (Ai9; JAX:007909) (Madisen et al., 2010), Tg(Nes-flpo/ERT2)1Alj (Nes-FlpoER; MGI:5532191) (Lao et al., 2012), Gad2¡tm1(cre/ERT2)Zjh¿ (Gad2-CreER, JAX:010702) (Taniguchi et al., 2011), Ai65(RCFL-tdT)-D (Ai65D, JAX:021875) (Madisen et al., 2015). Embryos were staged in days post-coitus, with e0.5 defined as 12:00 of the day a vaginal plug was detected after overnight mating.

scRNA-seq ($\star$) datasets: sample and library preparation

Three to six brains from Dlx5/6-Cre::tdTomato mouse embryos were collected at e12.5, e14.5 or e16.5 in ice-cold L-15 medium containing 5% FBS. Ganglionic eminences were manually dissected and dissociated with the Miltenyi Bio Tech Neural Tissue Dissociation Kit (P) (#130-092-628) on a gentleMACS Dissociator according to the manufacturer's protocol. From the same brains, cortical and striatal regions were dissected, dissociated, and FACS-enriched for tdTomato-positive cells using a SY3200 Cell Sorter (software WinList3D version 8.0.2) or BD FACSAria III Cell Sorter (BD FACSDiva Software, version 8.0.2) with a 100 μm nozzle. TdTomato-positive neurons from the cortex and striatum were pooled with neurons from the GEs, and scRNA-seq was performed. For experiments employing the 10x Genomics platform, Chromium Single Cell 3' Library & Gel Bead Kit v3 (PN-1000075), Chromium Single Cell 3' Chip Kit v3 (PN-1000073), and Chromium i7

Multiplex Kit (PN-120262) were used according to the manufacturer's instructions. Additionally, Chromium Single Cell 3' Library & Gel Bead Kit v3.1 (PN-1000268), Chromium Single Cell 3' Chip Kit v3.1 (PN-1000127), and Dual Index Kit TT Set A (PN-1000215) were used according to the manufacturer's instructions in the Chromium Single Cell 3' Reagents Kits v3.1 User Guide (Dual Index). Libraries were quantified using a BioAnalyzer (Agilent) and sequenced either on an Illumina NextSeq500 or Novaseq at the Genomics Core Facility of the Helmholtz Center, at the Next Generation Facility of the Max Planck Institute of Biochemistry, or at MLL Münchner Leukämielabor GmbH.

TrackerSeq (▲) datasets: sample and library preparation

Timed pregnant mice were anaesthetised with isoflurane (5% induction, 3% during the surgery) and treated with the analgesic Metamizol (WDT). In *in utero* electroporation (IUE) of the TrackerSeq library was performed at e16.5 as previously described in (Bandler et al., 2022). Embryos were injected unilaterally in the lateral ventricle with 700 nL of DNA plasmid solution made of 0.5 $\mu\mathrm{g}\,\mu\mathrm{L}^{-1}$ pEF1a-pBase (piggyBac-transposase) and the TrackerSeq library 0.5 $\mu\mathrm{g}\,\mu\mathrm{L}^{-1}$, diluted in endo-free TE buffer and 0.002% Fast Green FCF (Sigma). Embryos were then electroporated with 5 electric pulses (50 V, 50 ms at 1 Hz) with a square-wave electroporator (BTX, ECM 830). The transcriptome libraries were prepared utilizing the 10x Genomics platform as previously described. The lineage barcode library retrieved from RNA was amplified with a standard NEB protocol for Q5 Hot Start High-Fidelity 2X Master Mix (#M094S) in a 50 $\mu\mathrm{L}$ reaction, using 10 $\mu\mathrm{L}$ of cDNA as a template. Specifically, each PCR contained the following: 25 $\mu\mathrm{L}$ Q5 High-fidelity 2X Master Mix, 2.5 $\mu\mathrm{L}$ 10 $\mu\mathrm{mol}$ P7 indexed reverse primer, 2.5 $\mu\mathrm{L}$ 10 $\mu\mathrm{mol}$ i5 indexed forward primer, 10 $\mu\mathrm{L}$ molecular-grade H2O, 10 $\mu\mathrm{L}$ cDNA. The PCR protocol for amplifying TrackerSeq lineage libraries was: (1) 98 °C for 30 s, (2) 98 °C for 10 s, (3) 63 °C for 20 s, (4) 72 °C for 10 s, (5) repeat steps 2–4 for 11 to 18 times, (6) 72 °C for 2 min, and (7) 4 °C hold. Libraries were purified with a dual-sided SPRI selection using Beckman Coulter Agencourt RNAClean XP beads (Beckman Coulter, A63987) and quantified with a BioAnalyzer.

FlashTag (■) transcriptome datasets: sample and library preparation

Timed pregnant mice were anaesthetised with isoflurane and treated with the analgesic Metamizol as previously described. A CFSE working solution was prepared by adding 8 µL of DMSO and 1 µL of Fast Green to one vial of CellTrace CFSE (CellTraceTM CFSE, Life Technologies, #C34554) for a final concentration of 10 mM, following the instructions from Govindan *et al.* (Govindan et al., 2018). For $FT_{e12.5+6h}$ and $FT_{e16.5+6h}$, 500 nL of CFSE working solution was injected into ventricles of wild-type C57BL/6NRj embryos at e12.5 and e16.5 respectively. The abdominal wall was then closed, and the embryos were left to develop until collection. After six hours, ganglionic eminences were manually dissected and dissociated on the gentleMACS Dissociator according to the manufacturer's protocol. FlashTag positive cells with high intensity (¿ 10^5) were sorted using FACS (Fig. S1g) and scRNA-seq was performed. For $FT_{e12.5+96h}$, 500 nL of CFSE working solution was injected into ventricles of Dlx5/6-Cre::tdTomato embryos at e12.5. After 96 hours, the striatum and cortex were dissected and dissociated on the gentleMACS Dissociator. FlashTag and tdTomato positive cells were sorted using FACS, and scRNA-seq was performed.

FlashTag (■) chromatin accessibility datasets: sample and library preparation

Sample preparation was performed as for $FT_{e12.5+6h}$ and $FT_{e16.5+6h}$ in the previous section. scATAC-seq was performed according to the Chromium Single Cell ATAC Reagent Kits v1 user guide (10x Genomics). FACS sorted cells were centrifuged at 500 rcf for 5 min at 4 °C and resuspended in 100 µL chilled diluted lysis buffer and incubated for 5 min at 4 °C. 1 ml of chilled wash buffer was added to the lysed cells and mixed five times with a pipette, followed by centrifugation at 500 rcf for 5 min at 4°C. The isolated nuclei were counted (using a c-chip hemocytometer) and resuspended in an appropriate volume of chilled diluted nuclei buffer to reach the desired final nuclei concentration. The nuclei were immediately used to generate single-cell ATAC libraries, followed by paired-end sequencing on the Illumina NextSeq 500 platform.

Transplantation datasets: sample and library preparation

To generate the $AP_{e12.5 \rightarrow e12.5}$, $AP_{e12.5 \rightarrow e16.5}$, $AP_{e16.5 \rightarrow e16.5}$, and $AP_{e16.5 \rightarrow e13.5}$ datasets, timed pregnant mice were anaesthetised with isoflurane and treated with the analgesic Metamizol as previously described. To target APs, injection of CFSE working solution was performed into wild type C57BL/6NRj embryos at e12.5 and e16.5. One hour later, APs were FT^+ and three to six embryonic brains were collected. After manual dissections of the ganglionic eminences in ice-cold L-15 medium containing 5% FBS, the tissue was dissociated on a gentleMACS dissociator according to the manufacturer's protocol. Cells were resuspended in ice-cold HBSS containing $10\,\mathrm{mmol}$ EGTA and 0.1% Fast Green to a final concentration of 40000 $\mathrm{cells/\mu L}$ to 80000 $\mathrm{cells/\mu L}$. The cell suspension was split into two separate pools, and 1 $\mu\mathrm{L}$ was injected homo- or hetero-chronically into the ventricles of embryonic brains at e12.5 or e16.5. Forty-eight hours later, ganglionic eminences were dissected and dissociated as described above. CFSE-labelled cells were isolated with flow cytometry and centrifuged 500 rpm, $5\,\mathrm{min}$, $4°\mathrm{C}$. Total RNA-seq libraries were prepared using the SMART-Seq® Stranded Kit (634442, Takara), according to standard manufacturer's protocol (Low-input Workflow, PCR 1: 5 cycles and PCR 2: 12–15 cycles). The library quality was assessed by using a Qubit™ Flex Fluorometer (Q33327, Thermo Fisher Scientific) and a 4200 TapeStation (G2991BA, Agilent). A total of 10 samples were multiplexed and sequenced in a lane of a NovaSeq 6000 SP flow cell with the 100 cycles kit for paired-end sequencing (2× 60 bp) to reduce sequencing batch effects (100 pM final loading, 42 M reads per sample on average). BCL raw data were converted to FASTQ data and demultiplexed by the bcl2fastq Conversion Software (Illumina).

Tamoxifen induction

Tamoxifen was dissolved in corn oil to generate a concentration of 20 $\mathrm{mg\,mL^{-1}}$ by constant stirring at $37°\mathrm{C}$. Mouse strains Nes-FlpoER$^{+/-}$, Gad2-CreER$^{+/-}$ and Ai65D$^{+/+}$ were crossed to obtain Nes-FlpoER::Gad2-CreER::Ai65D embryos. At e12.5 and e16.5 100 $\mathrm{mg\,kg^{-1}}$ of tamoxifen was administered to the pregnant dam by gavage. The embryos were allowed to develop until collection

at P8.

scRNA-seq (⋆), TrackerSeq (▲), and FlashTag (■) transcriptome datasets: pre-processing and merging

Sequencing reads were processed using CellRanger v3.0.2 or v6.1.2 (Zheng et al., 2017), using the mouse reference genome mm10 v2.1.0. Resulting count matrices were analysed using the Seurat package v4.3.0 (Hao et al., 2021) in R v4.1.0. For each dataset, high-quality cells were filtered by the number of genes and mitochondrial read fraction (Fig. 3a,b). Subsequently, counts were normalized and corrected for sequencing depth using Seurat's *NormalizeData* function. Cell-cycle assignments for each cell were calculated using the cell-cycle gene list from (Tirosh et al., 2016). After identification of highly variable features as described in (Butler et al., 2018), we calculated scaled gene-expression values by applying z-normalisation to the 2000 most variable genes, whilst simultaneously regressing out unwanted sources of variation: sequencing-depth, feature-depth, mitochondrial read fraction and estimated difference between cell-cycle phases (*ScaleData* function). The *FindClusters* function was used to identify cell clusters. The *FindAllMarkers* function was used to identify cluster marker genes. Clusters with marker genes of excitatory neurons (e.g. Neurod1, Neurod6, Tbr2) or non-neuronal cells (e.g. Apoe, Olig1, Flt1, Pdgfra) were filtered out and excluded from the following steps. Raw counts of samples from scRNASeq, TrackerSeq, and FlashTag datasets were merged using the Seurat package and aligned using Monocle3 v1.0.0 (Trapnell et al., 2014; Qiu et al., 2017; Cao et al., 2019). For this purpose, the scaled matrix from the Seurat object was converted into a Monocle3 object of the cell_data_set class and preprocessed without the default normalisation, as the dataset was already normalised. Batch-correction was performed using Batchelor v1.8.1 (Haghverdi et al., 2018) followed by Leiden-clustering (using fine resolution) and dimensional reduction using UMAP (McInnes et al., 2020). A developmental trajectory was fitted as a principal graph through fine clusters based on the UMAP-embedding. The root of the trajectory was defined as the cells with the highest Nestin gene expression, identified in the "Fabp7" cluster. A pseudotime score was assigned to each cell based on its projected position on the trajectory.

Leiden clustering (using coarser resolution in Monocle3) identified distinct clusters of cell states. Marker genes specific to each cluster were identified by running differential expression analysis (in Seurat) using the *FindAllMarkers* function. Clusters were manually annotated based on marker gene expression. The transition between mitotic and postmitotic cells was defined by selecting the highest pseudotime score of mitotic clusters as the threshold.

scRNASeq (⋆) datasets and published datasets: analysis

We downloaded raw counts of e13.5 and e15.5 datasets from (Bandler et al., 2022) (GSE IDs: GSM5684874, GSM5684875, GSM5684876, GSM5684877, GSM5684878, and GSM5684879) and raw counts from the developing mouse somatosensory cortex (Di Bella et al., 2021) at stages e12.5 to e16.5 (GSE IDs: GSM4635073, GSM4635074, GSM4635075, GSM4635076, and GSM4635077). The count matrices were merged with our scRNASeq (⋆) datasets to create a combined Seurat object. We filtered cells based on mitochondrial read fraction ($\leq 10\%$). Normalization, scaling, batch correction, dimensionality reduction, and clustering were performed as previously described. Clusters were manually annotated based on top marker gene expression. For cells originating from Di Bella *et al.*, we utilized the annotations available from the original paper (Di Bella et al., 2021).

We screened for genes that are variable along the pseudotime in inhibitory and excitatory lineages with the following steps: (1) For each lineage, we binned cells from each stage into ten sections based on their inferred pseudotime. (2) Enriched genes were selected based on two criteria: high expression and high gene abundance. High expression was inferred by calculating the fold change between the expression in all cells inside the bin compared to all cells outside the bin. High gene abundance was calculated by comparing the fraction of cells that express a gene inside versus outside the bin (a gene was considered to be expressed in a cell if its scaled expression value was higher than 0.5). (3) A normal distribution was fitted to the changes in expression and abundance. Significantly enriched genes were selected when the difference in expression and abundance was higher than the corresponding average difference plus two times the standard deviation of the corresponding fitted distribution. (4) Steps two and three were repeated for each bin. (5) The trajectory of inhibitory

neurons branches out as cells leave the cell cycle, therefore we ran this algorithm for each branch independently and only considered genes that appeared in at least two out of five branches. (6) Finally, by taking the union of dynamic genes of all stages in inhibitory or excitatory lineages, we created a stable set of genes that are dynamic along pseudotime, but conserved across stages.

TrackerSeq (▲) datasets: analysis

TrackerSeq barcode reads were pre-processed as described in Bandler *et al.* (Bandler et al., 2022). To assess the clonal coupling between cell states, we calculated z-scores between clusters (Wagner et al., 2018). The z-score is defined as the number of shared barcodes relative to randomized data, with values ranging from positive (coupled clusters) to negative (anticoupled clusters). We utilized these random permutations to calculate empirical *P*-values. For coupled pairs of clusters, the null hypothesis is that the observed coupling is not higher than random coupling. Conversely, for anticoupled pairs, the null hypothesis is that the observed coupling is not lower than random couplings. A random coupling is in contradiction to the null hypothesis when a permutation for one pair of clusters scores above the observed coupling (for positively coupled pairs), or below the observed coupling (for negatively coupled pairs). The relative fraction is reflected in the empirical *P*-value, which was consequently corrected for multiple comparisons using the Benjamini-Hochberg (FDR) method (Benjamini and Hochberg, 1995).

Clones were identified as ”dispersing” or ”non-dispersing” depending on whether their cells were distributed in multiple or just one branch tip, respectively. We tested whether the transcriptome of mitotic progenitors in ”non-dispersing” clones was predictive of their postmitotic state. ”Non-dispersing” clones were grouped by their postmitotic cell state in both $\text{TrackerSeq}_{\text{e12.5 + 96h}}$ and $\text{TrackerSeq}_{\text{e16.5 + 96h}}$ combined. Separate data frames were created for mitotic and postmitotic subsets of each group. Pearson correlation coefficients were calculated between pairs of gene expression within different subsets, generating all the possible combinations of pairs within the columns of the data frames. The subsets of postmitotic clones, mitotic clones, and randomly selected mitotic cells were all correlated to the postmitotic reference group.

FlashTag chromatin datasets: analysis

The raw sequencing data (BCL file) were converted to the fastq format using *cellranger-atac mkfastq* function from Cell Ranger ATAC v1.2.0 (Satpathy et al., 2019). The reads were aligned to the mm10 (GRCm38) mouse reference genome and fragment files were generated using the *cellranger-atac count* function. Both time points included 2 replicates (Fig. S11a), and the aligned fragment files were converted to arrow files and analysed further using the ArchR package v1.0.1 (Granja et al., 2021). Dimensionality reduction was performed using latent semantic indexing (LSI), followed by batch correction using Harmony v0.1.1 (Korsunsky et al., 2019). To extract the trajectories of interest and integrate them into a ArchRProject, we employed the *getTrajectory* and *addTrajectory* functions, respectively. To visualize enriched motifs, we generated pseudotime heatmaps.

FlashTag chromatin datasets: temporal dynamics and coverage plots

Peak calling was performed using *addReproduciblePeakSet* function, which runs MACS2 (Zhang et al., 2008) to identify marker peaks for $FT_{e12.5+6h}$ and $FT_{e16.5+6h}$ datasets. To categorize peak sets into unique and overlapping peaks, we utilized the *findoverlap* function. For both scATAC-seq and H3K4me3 ChIP-seq datasets, we calculated peak coverage for each peak category using the *ScoreMatrixList* function.

FlashTag chromatin datasets: transcription factor footprint analysis

Footprint analysis was carried out on $FT_{e12.5+6h}$ and $FT_{e16.5+6h}$ datasets using transcription factor occupancy prediction tool: TOBIAS v0.14.0 (Bentsen et al., 2020). We employed the Jaspar non-redundant motif database (Castro-Mondragon et al., 2022) as the primary reference source for motif data. Bias correction was performed to generate corrected bigwig files using the *ATACCorrect* function with default parameters. Footprint scores were calculated on corrected bigwig files using the *FootprintScores* function, and differential binding TFs were detected using *BINDetect* function. Predicted TFs were categorised as significant based on two criteria: their differential binding score

601 (greater than 0.2 for e12.5 and less than –0.4 for e16.5:referred to as change) and the –log10 of the
602 p-value from the statistical test against a background model. The footprints were visualized using
603 the *PlotAggregate* and *PlotHeatmap* functions.

604 FlashTag chromatin datasets: co-binding analysis

605 To detect co-occurring TF binding sites, we utilized TF-COMB v1.1 (Bentsen et al., 2022). A
606 distinct CombObj was created by loading unique peak sets (e12.5 and e16.5) identified previously.
607 Transcription factor binding sites were identified within the peak regions followed by market basket
608 analysis. TFs co-occurring with NFIB were then subsetted and further assessed for their co-binding
609 (cosine score) and binding events via dot plot.

610 FlashTag transcriptome and chromatin datasets: gene regulatory network 611 prediction

612 We used Scenic+ (v0.1) (Gonzalez-Blas et al., 2023) to predict GRNs for CFSE-labelled cells
613 at e12.5 and e16.5. As scRNA-seq and scATAC-seq data were unpaired we created a common
614 annotation, by defining broad cell states (AP, BP, and precursor) in the transcriptomic data, merging
615 clusters based on marker gene expression. Annotations in the scATAC-seq data were created by
616 applying label transfer, based on gene-scores predicted by ArchR. These broad cell states were split
617 by stage, resulting in 6 stage-specific cell states (Fig. S12a). Scenicplus performs co-accessibility
618 analysis of regions and links regions to upstream TFs by searching for enriched TF motifs in regions.
619 To make this analysis more coherent with prior results, we used the previously calculated peak-set
620 from ArchR as input for Scenicplus, instead of recalculating a new peak-set using pycisTopic (Bravo
621 González-Blas et al., 2019). Following the Scenicplus workflow, we created topics of co-accessible
622 regions and performed binarization and motif enrichment of regions in the 20 most important topics.
623 Networks were created by aggregating 10 cells from both modalities of corresponding cell states into
624 pseudocells and then inferring TFs and regions that are predictive of a gene, based on co-accessibility

and motif enrichment. The regions considered for a gene have to lie within a genomic interval of 150 kb up- and downstream of the gene. The results are so-called ”eRegulons”, i.e. regulatory triplets of one TF, bound regions and corresponding target genes. For each eRegulon the activity in each cell was calculated using AUC-scores (Aibar et al., 2017). Each eRegulon was filtered using standard filtering (*apply_std_filtering_to_eRegulons* function) and high quality eRegulons were selected by filtering for eRegulons where TF-expression and AUC scores correlated more than 0.5 or less than -0.5.

We reconstructed cell-state specific subnetworks by running AUC-binarization (*binarize_AUC*-function). Here, we filtered for (1) eRegulons that are active in at least 50% of cells within a corresponding cell state and for (2) corresponding target genes that have a higher normalized expression than 0.5 (normalized expression is log1p transformed after correcting for sequencing depth). Cell state specific networks (APs, BPs and precursors) were created by merging the corresponding e12.5- and e16.5-subnetwork using the igraph library v1.5.0 (Csardi and Nepusz, 2006). Stage specific networks (e12.5 and e16.5) are similarly created by merging subnetworks of APs, BPs, and precursors of the same stage. In both approaches, the merged networks consisted of the union of vertices and edges. GO-enrichment analysis of target genes was performed using DAVID with default parameters (Dennis et al., 2003).

Transplantation datasets: analysis

We used the Galaxy web platform on the public server at usegalaxy.eu to analyse the data (Afgan et al., 2018). Paired end reads were trimmed with the Trimmomatic tool and quality control was performed with FastQC. Reads were mapped to the mouse reference genome using the HISAT2 algorithm (Kim et al., 2019) and the number of reads per annotated genes was counted using featureCounts (Liao et al., 2014). After Fragments Per Kilobase of transcript per Million mapped reads (fpkm) normalization of the count matrices, the proportion of single cell states within each replicate was inferred with Bisque v1.0.5 (Jew et al., 2020) by using the annotated combined single-cell clusters as reference. A weighted pseudotime score was assigned to each replicate by calculating the median

of the pseudotime score per cluster from the combined single cell datasets. For differential gene expression analysis, the count matrices were subset by variable genes of inhibitory neuron datasets and DESeq2 v1.42.0 was utilized (Love et al., 2014).

Whole-cell patch-clamp recordings

Acute striatal slices ($300\,\mu m$ thick) were obtained from triple transgenic mice at P8 of pregnant mice after tamoxifen gavage at e12.5 and e16.5. Mice were decapitated, and brains were rapidly removed and placed in a carbogenated (95% O_2/5% CO_2) N-methyl-D-glucamine-based artificial cerebrospinal fluid (NMDG-aCSF) solution containing the following (in $mmol\,L^{-1}$): 92 NMDG, 2.5 KCl, 1.2 NaH_2PO_4, 30 $NaHCO_3$, 20 HEPES, 25 glucose, 5 sodium ascorbate, 2 thiourea, 3 sodium pyruvate, 10 $MgSO_4{\cdot}7H_2O$, and 0.5 $CaCl_2{\cdot}2H_2O$ (pH 7.2–7.4, 300–310 mOsm). Slices were cut using a VT1000S vibratome (Leica Microsystems) and then incubated for 11 min at 32–34 $^{\circ}C$ with carbogenated NMDG-aCSF solution, followed by at least one-hour recovery at RT in an aCSF solution containing the following (in $mmol\,L^{-1}$): 119 NaCl, 2.5 KCl, 1.2 NaH_2PO_4, 24 $NaHCO_3$, 12.5 glucose, 2 $MgSO_4{\cdot}7H_2O$, and 2 $CaCl_2{\cdot}2H2O$ (pH 7.2–7.4, 300–310 mOsm).

Recording pipettes were pulled from BF150-110-7.5HP borosilicate glass capillaries (Science Products) on a P97 horizontal puller (Sutter Instruments) with a typical resistance of 2–5 $M\Omega$. Pipettes were filled with K-gluconate internal solution containing the following (in $mmol\,L^{-1}$): 135 K-gluconate, 4 KCl, 2 NaCl, 10 HEPES, 0.2 EGTA, 4 MgATP, 0.5 NaGTP, and 10 phosphocreatine (adjusted to pH 7.3 with KOH and 290 mOsm with sucrose). Biocytin (0.5%) was added to the electrode solution, and the pipettes were backfilled to minimize background fluorescence.

Whole-cell patch-clamp recordings were performed after seal rupture under a SliceScope upright microscope (Scientifica) equipped with epifluorescence and infrared differential interference contrast (IR-DIC) optics. All recordings were performed at RT (22–25 $^{\circ}C$) from fluorescently labelled neurons located in the dorsal striatum. Intrinsic properties were measured using the voltage response to a series of hyperpolarizing and depolarizing current injections ($10\,pA$ steps, starting at $-150\,pA$). Rheobase current was defined as the smallest positive current step capable of eliciting at least one

action potential. Input resistance was calculated with a $-150\,\mathrm{pA}$ hyperpolarizing step from the resting membrane potential and from a linear fit to a voltage-current plot. Whole-cell capacitance was measured using a $5\,\mathrm{mV}$, $200\,\mathrm{ms}$ step from $-90\,\mathrm{mV}$, with a 4-pole Bessel filter with a cutoff frequency of $10\,\mathrm{kHz}$. A bi-exponential fit of membrane response following the $5\,\mathrm{mV}$ depolarization was used to calculate the weighted tau and consequent whole-cell capacitance as described by Gertler *et al.* (Gertler et al., 2008).

Data were acquired using a MultiClamp 700B amplifier and digitized using a Digidata 1550B acquisition system (Molecular Devices). Signals were further filtered at $2\,\mathrm{kHz}$ and digitized at $10\,\mathrm{kHz}$. For current-clamp recordings, the bridge balance was adjusted and pipette capacitance was neutralized. pClamp 11 software was used for analysis (Clampfit, Axon Instruments).

Dendritic reconstruction

For anatomical reconstruction, brain slices containing biocytin-filled neurons were post-fixed in 4% paraformaldehyde for 12 h at 4 °C. After fixation, slices were washed 3 times in phosphate buffer saline (PBS, pH 7.5) and permeabilized with PBS containing 0.2% Triton-X100 for 24 h at 4 °C. Following 5 washes for 10 min in PBS, biocytin localization was visualized by incubating the slices in Alexa 488-coupled streptavidin (diluted 1:1000 in PBS, Molecular Probes) for 48 h at 4 °C. Slices were washed a further 5 times in PBS and mounted on Superfrost slices (ThermoFisher Scientific). Z-stack serial images were acquired on a SP8 Leica confocal microscope (Leica Microsystems) using a 40× oil immersion objective. Neuronal arbour reconstruction and analysis were carried out using the Simple Neurite Tracer (SNT) plugin in the Fiji ImageJ package (https://imagej.net/Fiji). Total neurite arbour size and branching were measured within Fiji ImageJ. The Sholl analysis was performed using the skeletonized neuron from SNT, with the centre of the cell body as the origin. No correction was applied for tissue shrinkage during fixation.

References

Adam, R. C., Yang, H., Ge, Y., Infarinato, N. R., Gur-Cohen, S., Miao, Y., Wang, P., Zhao, Y., Lu, C. P., Kim, J. E., Ko, J. Y., Paik, S. S., Gronostajski, R. M., Kim, J., Krueger, J. G., Zheng, D., and Fuchs, E. (2020). Nfi transcription factors provide chromatin access to maintain stem cell identity while preventing unintended lineage fate choices. *Nat Cell Biol*, 22(6):640–650.

Afgan, E., Baker, D., Batut, B., van den Beek, M., Bouvier, D., Cech, M., Chilton, J., Clements, D., Coraor, N., Grüning, B. A., Guerler, A., Hillman-Jackson, J., Hiltemann, S., Jalili, V., Rasche, H., Soranzo, N., Goecks, J., Taylor, J., Nekrutenko, A., and Blankenberg, D. (2018). The galaxy platform for accessible, reproducible and collaborative biomedical analyses: 2018 update. *Nucleic Acids Res*, 46(W1):W537–W544.

Aibar, S., González-Blas, C. B., Moerman, T., Huynh-Thu, V. A., Imrichova, H., Hulselmans, G., Rambow, F., Marine, J.-C., Geurts, P., Aerts, J., van den Oord, J., Atak, Z. K., Wouters, J., and Aerts, S. (2017). SCENIC: single-cell regulatory network inference and clustering. *Nature Methods*, 14(11):1083–1086. Bandiera_abtest: a Cg_type: Nature Research Journals Number: 11 Primary_atype: Research Publisher: Nature Publishing Group Subject_term: Gene regulatory networks;RNA sequencing;Transcriptomics;Tumour heterogeneity Subject_term_id: gene-regulatory-networks;rna-sequencing;transcriptomics;tumour-heterogeneity.

Allaway, K. C., Gabitto, M. I., Wapinski, O., Saldi, G., Wang, C.-Y., Bandler, R. C., Wu, S. J., Bonneau, R., and Fishell, G. (2021). Genetic and epigenetic coordination of cortical interneuron development. *Nature*, 597(7878):693–697.

Anderson, S. A., Marin, O., Horn, C., Jennings, K., and Rubenstein, J. L. (2001). Distinct cortical migrations from the medial and lateral ganglionic eminences. *Development*, 128(3):353–63.

Bandler, R. C., Vitali, I., Delgado, R. N., Ho, M. C., Dvoretskova, E., Ibarra Molinas, J. S., Frazel, P. W., Mohammadkhani, M., Machold, R., Maedler, S., Liddelow, S. A., Nowakowski, T. J., Fishell, G., and Mayer, C. (2022). Single-cell delineation of lineage and genetic identity in the mouse brain. *Nature*, 601(7893):404–409.

Benjamini, Y. and Hochberg, Y. (1995). Controlling the False Discovery Rate: A Practical and Powerful Approach to Multiple Testing. *Journal of the Royal Statistical Society: Series B (Methodological)*, 57(1):289–300. _eprint: https://onlinelibrary.wiley.com/doi/pdf/10.1111/j.2517-6161.1995.tb02031.x.

Bentsen, M., Goymann, P., Schultheis, H., Klee, K., Petrova, A., Wiegandt, R., Fust, A., Preussner, J., Kuenne, C., Braun, T., Kim, J., and Looso, M. (2020). Atac-seq footprinting unravels kinetics of transcription factor binding during zygotic genome activation. *Nat Commun*, 11(1):4267.

Bentsen, M., Heger, V., Schultheis, H., Kuenne, C., and Looso, M. (2022). Tf-comb - discovering grammar of transcription factor binding sites. *Comput Struct Biotechnol J*, 20:4040–4051.

Bertacchi, M., Romano, A. L., Loubat, A., Tran Mau-Them, F., Willems, M., Faivre, L., Khau van Kien, P., Perrin, L., Devillard, F., Sorlin, A., Kuentz, P., Philippe, C., Garde, A., Neri, F., Di Giaimo, R., Oliviero, S., Cappello, S., D'Incerti, L., Frassoni, C., and Studer, M. (2020). NR2F1 regulates regional progenitor dynamics in the mouse neocortex and cortical gyrification in BBSOAS patients. *The EMBO Journal*, 39(13):e104163.

Betancourt, J., Katzman, S., and Chen, B. (2014). Nuclear factor one b regulates neural stem cell differentiation and axonal projection of corticofugal neurons. *J Comp Neurol*, 522(1):6–35.

Bonnefont, J. and Vanderhaeghen, P. (2021). Neuronal fate acquisition and specification: time for a change. *Curr Opin Neurobiol*, 66:195–204.

Bravo González-Blas, C., Minnoye, L., Papasokrati, D., Aibar, S., Hulselmans, G., Christiaens, V., Davie, K., Wouters, J., and Aerts, S. (2019). cisTopic: cis-regulatory topic modeling on single-cell ATAC-seq data. *Nature Methods*, 16(5):397–400. Number: 5 Publisher: Nature Publishing Group.

Buenrostro, J. D., Wu, B., Chang, H. Y., and Greenleaf, W. J. (2015). Atac-seq: A method for assaying chromatin accessibility genome-wide. *Curr Protoc Mol Biol*, 109:21.29.1–21.29.9.

Bunt, J., Osinski, J. M., Lim, J. W., Vidovic, D., Ye, Y., Zalucki, O., O'Connor, T. R., Harris, L., Gronostajski, R. M., Richards, L. J., and Piper, M. (2017). Combined allelic dosage of nfia and nfib regulates cortical development. *Brain Neurosci Adv*, 1:2398212817739433.

Butler, A., Hoffman, P., Smibert, P., Papalexi, E., and Satija, R. (2018). Integrating single-cell transcriptomic data across different conditions, technologies, and species. *Nature biotechnology*, 36(5):411–420.

Butt, S. J. B., Sousa, V. H., Fuccillo, M. V., Hjerling-Leffler, J., Miyoshi, G., Kimura, S., and Fishell, G. (2008). The requirement of nkx2-1 in the temporal specification of cortical interneuron subtypes. *Neuron*, 59(5):722–32.

Cao, J., Spielmann, M., Qiu, X., Huang, X., Ibrahim, D. M., Hill, A. J., Zhang, F., Mundlos, S., Christiansen, L., Steemers, F. J., Trapnell, C., and Shendure, J. (2019). The single-cell transcriptional landscape of mammalian organogenesis. *Nature*, 566(7745):496–502.

Castro-Mondragon, J. A., Riudavets-Puig, R., Rauluseviciute, I., Lemma, R. B., Turchi, L., Blanc-Mathieu, R., Lucas, J., Boddie, P., Khan, A., Manosalva Pérez, N., Fornes, O., Leung, T. Y., Aguirre, A., Hammal, F., Schmelter, D., Baranasic, D., Ballester, B., Sandelin, A., Lenhard, B., Vandepoele, K., Wasserman, W. W., Parcy, F., and Mathelier, A. (2022). Jaspar 2022: the 9th release of the open-access database of transcription factor binding profiles. *Nucleic Acids Res*, 50(D1):D165–D173.

Chávez, S. and Beato, M. (1997). Nucleosome-mediated synergism between transcription factors on the mouse mammary tumor virus promoter. *Proc Natl Acad Sci U S A*, 94(7):2885–90.

Ciceri, G., Baggiolini, A., Cho, H. S., Kshirsagar, M., Benito-Kwiecinski, S., Walsh, R. M., Aromolaran, K. A., Gonzalez-Hernandez, A. J., Munguba, H., Koo, S. Y., Xu, N., Sevilla, K. J., Goldstein, P. A., Levitz, J., Leslie, C. S., Koche, R. P., and Studer, L. (2024). An epigenetic barrier sets the timing of human neuronal maturation. *Nature*.

Clark, B. S., Stein-O'Brien, G. L., Shiau, F., Cannon, G. H., Davis-Marcisak, E., Sherman, T., Santiago, C. P., Hoang, T. V., Rajaii, F., James-Esposito, R. E., Gronostajski, R. M., Fertig, E. J., Goff, L. A., and Blackshaw, S. (2019). Single-cell rna-seq analysis of retinal development identifies nfi factors as regulating mitotic exit and late-born cell specification. *Neuron*, 102(6):1111–1126.e5.

Colasante, G., Simonet, J. C., Calogero, R., Crispi, S., Sessa, A., Cho, G., Golden, J. A., and Broccoli, V. (2015). ARX Regulates Cortical Intermediate Progenitor Cell Expansion

and Upper Layer Neuron Formation Through Repression of Cdkn1c. *Cerebral Cortex*, 25(2):322–335.

Corbin, J. G., Nery, S., and Fishell, G. (2001). Telencephalic cells take a tangent: non-radial migration in the mammalian forebrain. *Nat Neurosci*, 4 Suppl:1177–82.

Csardi, G. and Nepusz, T. (2006). The igraph software package for complex network research. *InterJournal*, Complex Systems:1695.

Dennis, G., Sherman, B. T., Hosack, D. A., Yang, J., Gao, W., Lane, H. C., and Lempicki, R. A. (2003). DAVID: Database for Annotation, Visualization, and Integrated Discovery. *Genome Biology*, 4(5):P3.

Di Bella, D. J., Habibi, E., Stickels, R. R., Scalia, G., Brown, J., Yadollahpour, P., Yang, S. M., Abbate, C., Biancalani, T., Macosko, E. Z., Chen, F., Regev, A., and Arlotta, P. (2021). Molecular logic of cellular diversification in the mouse cerebral cortex. *Nature*, 595(7868):554–559.

Dvoretskova, E., Ho, M. C., Kittke, V., Vitali, I., Delgado, I., Feng, C., Torres, M., Winkelmann, J., and Mayer, C. (2023). Spatial-specific enhancer activation determines inhibitory identity. *bioRxiv*.

Farnsworth, D. R. and Doe, C. Q. (2017). Opportunities lost and gained: Changes in progenitor competence during nervous system development. *Neurogenesis (Austin)*, 4(1):e1324260.

Flames, N., Pla, R., Gelman, D. M., Rubenstein, J. L. R., Puelles, L., and Marín, O. (2007). Delineation of multiple subpallial progenitor domains by the combinatorial expression of transcriptional codes. *J Neurosci*, 27(36):9682–95.

Flandin, P., Kimura, S., and Rubenstein, J. L. R. (2010). The progenitor zone of the ventral medial ganglionic eminence requires nkx2-1 to generate most of the globus pallidus but few neocortical interneurons. *J Neurosci*, 30(8):2812–23.

Fleck, J. S., Jansen, S. M. J., Wollny, D., Seimiya, M., Zenk, F., Santel, M., He, Z., Camp, J. G., and Treutlein, B. (2021). Inferring and perturbing cell fate regulomes in human cerebral organoids. Technical report. Company: Cold Spring Harbor Laboratory Distributor: Cold Spring Harbor Laboratory Label: Cold Spring Harbor Laboratory Section: New Results Type: article.

Fogarty, M., Grist, M., Gelman, D., Marín, O., Pachnis, V., and Kessaris, N. (2007). Spatial genetic patterning of the embryonic neuroepithelium generates gabaergic interneuron diversity in the adult cortex. *J Neurosci*, 27(41):10935–46.

Fragkouli, A., van Wijk, N. V., Lopes, R., Kessaris, N., and Pachnis, V. (2009). Lim homeodomain transcription factor-dependent specification of bipotential mge progenitors into cholinergic and gabaergic striatal interneurons. *Development*, 136(22):3841–51.

Gelman, D., Griveau, A., Dehorter, N., Teissier, A., Varela, C., Pla, R., Pierani, A., and Marín, O. (2011). A wide diversity of cortical gabaergic interneurons derives from the embryonic preoptic area. *J Neurosci*, 31(46):16570–80.

Gertler, T. S., Chan, C. S., and Surmeier, D. J. (2008). Dichotomous anatomical properties of adult striatal medium spiny neurons. *J Neurosci*, 28(43):10814–24.

Glickstein, S. B., Moore, H., Slowinska, B., Racchumi, J., Suh, M., Chuhma, N., and Ross, M. E. (2007). Selective cortical interneuron and gaba deficits in cyclin d2-null mice. *Development*, 134(22):4083–93.

Gonzalez-Blas, C. B., De Winter, S., Hulselmans, G., Hecker, N., Matetovici, I., Christiaens, V., Poovathingal, S., Wouters, J., Aibar, S., and Aerts, S. (2023). Scenic+: single-cell multiomic inference of enhancers and gene regulatory networks. *Nature Methods*.

Gorkin, D. U., Barozzi, I., Zhao, Y., Zhang, Y., Huang, H., Lee, A. Y., Li, B., Chiou, J., Wildberg, A., Ding, B., Zhang, B., Wang, M., Strattan, J. S., Davidson, J. M., Qiu, Y., Afzal, V., Akiyama, J. A., Plajzer-Frick, I., Novak, C. S., Kato, M., Garvin, T. H., Pham, Q. T., Harrington, A. N., Mannion, B. J., Lee, E. A., Fukuda-Yuzawa, Y., He, Y., Preissl, S., Chee, S., Han, J. Y., Williams, B. A., Trout, D., Amrhein, H., Yang, H., Cherry, J. M., Wang, W., Gaulton, K., Ecker, J. R., Shen, Y., Dickel, D. E., Visel, A., Pennacchio, L. A., and Ren, B. (2020). An atlas of dynamic chromatin landscapes in mouse fetal development. *Nature*, 583(7818):744–751.

Götz, M. and Huttner, W. B. (2005). The cell biology of neurogenesis. *Nat Rev Mol Cell Biol*, 6(10):777–88.

Govindan, S., Oberst, P., and Jabaudon, D. (2018). In vivo pulse labeling of isochronic cohorts of cells in the central nervous system using flashtag. *Nat Protoc*, 13(10):2297–2311.

Granja, J. M., Corces, M. R., Pierce, S. E., Bagdatli, S. T., Choudhry, H., Chang, H. Y., and Greenleaf, W. J. (2021). Archr is a scalable software package for integrative single-cell chromatin accessibility analysis. *Nat Genet*, 53(3):403–411.

Haghverdi, L., Lun, A. T. L., Morgan, M. D., and Marioni, J. C. (2018). Batch effects in single-cell RNA sequencing data are corrected by matching mutual nearest neighbours. *Nature biotechnology*, 36(5):421–427.

Hao, Y., Hao, S., Andersen-Nissen, E., Mauck, W. M., Zheng, S., Butler, A., Lee, M. J., Wilk, A. J., Darby, C., Zager, M., Hoffman, P., Stoeckius, M., Papalexi, E., Mimitou, E. P., Jain, J., Srivastava, A., Stuart, T., Fleming, L. M., Yeung, B., Rogers, A. J., McElrath, J. M., Blish, C. A., Gottardo, R., Smibert, P., and Satija, R. (2021). Integrated analysis of multimodal single-cell data. *Cell*, 184(13):3573–3587.e29.

Harris, L., Zalucki, O., Gobius, I., McDonald, H., Osinki, J., Harvey, T. J., Essebier, A., Vidovic, D., Gladwyn-Ng, I., Burne, T. H., Heng, J. I., Richards, L. J., Gronostajski, R. M., and Piper, M. (2016). Transcriptional regulation of intermediate progenitor cell generation during hippocampal development. *Development*, 143(24):4620–4630.

Heintzman, N. D., Stuart, R. K., Hon, G., Fu, Y., Ching, C. W., Hawkins, R. D., Barrera, L. O., Van Calcar, S., Qu, C., Ching, K. A., Wang, W., Weng, Z., Green, R. D., Crawford, G. E., and Ren, B. (2007). Distinct and predictive chromatin signatures of transcriptional promoters and enhancers in the human genome. *Nat Genet*, 39(3):311–8.

Heng, Y. H. E., Barry, G., Richards, L. J., and Piper, M. (2012). Nuclear factor i genes regulate neuronal migration. *Neurosignals*, 20(3):159–67.

Hickey, S. L., Berto, S., and Konopka, G. (2019). Chromatin decondensation by foxp2 promotes human neuron maturation and expression of neurodevelopmental disease genes. *Cell Rep*,

27(6):1699–1711.e9.

Inan, M., Welagen, J., and Anderson, S. A. (2012). Spatial and temporal bias in the mitotic origins of somatostatin- and parvalbumin-expressing interneuron subgroups and the chandelier subtype in the medial ganglionic eminence. *Cereb Cortex*, 22(4):820–7.

Iwata, R., Casimir, P., Erkol, E., Boubakar, L., Planque, M., Gallego López, I. M., Ditkowska, M., Gaspariunaite, V., Beckers, S., Remans, D., Vints, K., Vandekeere, A., Poovathingal, S., Bird, M., Vlaeminck, I., Creemers, E., Wierda, K., Corthout, N., Vermeersch, P., Carpentier, S., Davie, K., Mazzone, M., Gounko, N. V., Aerts, S., Ghesquière, B., Fendt, S.-M., and Vanderhaeghen, P. (2023). Mitochondria metabolism sets the species-specific tempo of neuronal development. *Science*, 379(6632):eabn4705.

Janssens, J., Aibar, S., Taskiran, I. I., Ismail, J. N., Spanier, K. I., González-Blas, C. B., Quan, X. J., Papasokrati, D., Hulselmans, G., Makhzami, S., Waegeneer, M. D., Christiaens, V., and Aerts, S. (2021). Decoding gene regulation in the fly brain. Technical report. Company: Cold Spring Harbor Laboratory Distributor: Cold Spring Harbor Laboratory Label: Cold Spring Harbor Laboratory Section: New Results Type: article.

Jew, B., Alvarez, M., Rahmani, E., Miao, Z., Ko, A., Garske, K. M., Sul, J. H., Pietiläinen, K. H., Pajukanta, P., and Halperin, E. (2020). Accurate estimation of cell composition in bulk expression through robust integration of single-cell information. *Nat Commun*, 11(1):1971.

Kelly, S. M., Raudales, R., He, M., Lee, J. H., Kim, Y., Gibb, L. G., Wu, P., Matho, K., Osten, P., Graybiel, A. M., and Huang, Z. J. (2018). Radial glial lineage progression and differential intermediate progenitor amplification underlie striatal compartments and circuit organization. *Neuron*, 99(2):345–361.e4.

Kim, D., Paggi, J. M., Park, C., Bennett, C., and Salzberg, S. L. (2019). Graph-based genome alignment and genotyping with hisat2 and hisat-genotype. *Nat Biotechnol*, 37(8):907–915.

Korsunsky, I., Millard, N., Fan, J., Slowikowski, K., Zhang, F., Wei, K., Baglaenko, Y., Brenner, M., Loh, P.-R., and Raychaudhuri, S. (2019). Fast, sensitive and accurate integration of single-cell data with harmony. *Nat Methods*, 16(12):1289–1296.

Lao, Z., Raju, G. P., Bai, C. B., and Joyner, A. L. (2012). Mastr: a technique for mosaic mutant analysis with spatial and temporal control of recombination using conditional floxed alleles in mice. *Cell Rep*, 2(2):386–96.

Lee, D. R., Rhodes, C., Mitra, A., Zhang, Y., Maric, D., Dale, R. K., and Petros, T. J. (2022). Transcriptional heterogeneity of ventricular zone cells in the ganglionic eminences of the mouse forebrain. *Elife*, 11.

Liao, Y., Smyth, G. K., and Shi, W. (2014). featurecounts: an efficient general purpose program for assigning sequence reads to genomic features. *Bioinformatics*, 30(7):923–30.

Lim, L., Pakan, J. M. P., Selten, M. M., Marques-Smith, A., Llorca, A., Bae, S. E., Rochefort, N. L., and Marín, O. (2018). Optimization of interneuron function by direct coupling of cell migration and axonal targeting. *Nat Neurosci*, 21(7):920–931.

Lindtner, S., Catta-Preta, R., Tian, H., Su-Feher, L., Price, J. D., Dickel, D. E., Greiner, V., Silberberg, S. N., McKinsey, G. L., McManus, M. T., Pennacchio, L. A., Visel, A., Nord,

A. S., and Rubenstein, J. L. R. (2019). Genomic resolution of dlx-orchestrated transcriptional circuits driving development of forebrain gabaergic neurons. *Cell Rep*, 28(8):2048–2063.e8.

Liodis, P., Denaxa, M., Grigoriou, M., Akufo-Addo, C., Yanagawa, Y., and Pachnis, V. (2007). Lhx6 activity is required for the normal migration and specification of cortical interneuron subtypes. *J Neurosci*, 27(12):3078–89.

Liu, R., Liu, H., Chen, X., Kirby, M., Brown, P. O., and Zhao, K. (2001). Regulation of csf1 promoter by the swi/snf-like baf complex. *Cell*, 106(3):309–18.

Lodato, S., Tomassy, G. S., De Leonibus, E., Uzcategui, Y. G., Andolfi, G., Armentano, M., Touzot, A., Gaztelu, J. M., Arlotta, P., Menendez de la Prida, L., and Studer, M. (2011). Loss of coup-tfi alters the balance between caudal ganglionic eminence- and medial ganglionic eminence-derived cortical interneurons and results in resistance to epilepsy. *J Neurosci*, 31(12):4650–62.

Love, M. I., Huber, W., and Anders, S. (2014). Moderated estimation of fold change and dispersion for rna-seq data with deseq2. *Genome Biol*, 15(12):550.

Madisen, L., Garner, A. R., Shimaoka, D., Chuong, A. S., Klapoetke, N. C., Li, L., van der Bourg, A., Niino, Y., Egolf, L., Monetti, C., Gu, H., Mills, M., Cheng, A., Tasic, B., Nguyen, T. N., Sunkin, S. M., Benucci, A., Nagy, A., Miyawaki, A., Helmchen, F., Empson, R. M., Knöpfel, T., Boyden, E. S., Reid, R. C., Carandini, M., and Zeng, H. (2015). Transgenic mice for intersectional targeting of neural sensors and effectors with high specificity and performance. *Neuron*, 85(5):942–58.

Madisen, L., Zwingman, T. A., Sunkin, S. M., Oh, S. W., Zariwala, H. A., Gu, H., Ng, L. L., Palmiter, R. D., Hawrylycz, M. J., Jones, A. R., Lein, E. S., and Zeng, H. (2010). A robust and high-throughput cre reporting and characterization system for the whole mouse brain. *Nat Neurosci*, 13(1):133–40.

Marín, O. and Rubenstein, J. L. (2001). A long, remarkable journey: tangential migration in the telencephalon. *Nat Rev Neurosci*, 2(11):780–90.

Matuzelski, E., Bunt, J., Harkins, D., Lim, J. W. C., Gronostajski, R. M., Richards, L. J., Harris, L., and Piper, M. (2017). Transcriptional regulation of Nfix by NFIB drives astrocytic maturation within the developing spinal cord. *Developmental Biology*, 432(2):286–297.

Mayer, C., Hafemeister, C., Bandler, R. C., Machold, R., Batista Brito, R., Jaglin, X., Allaway, K., Butler, A., Fishell, G., and Satija, R. (2018). Developmental diversification of cortical inhibitory interneurons. *Nature*, 555(7697):457–462.

McInnes, L., Healy, J., and Melville, J. (2020). UMAP: Uniform Manifold Approximation and Projection for Dimension Reduction. *arXiv:1802.03426 [cs, stat]*. arXiv: 1802.03426.

Mi, D., Li, Z., Lim, L., Li, M., Moissidis, M., Yang, Y., Gao, T., Hu, T. X., Pratt, T., Price, D. J., Sestan, N., and Marin, O. (2018). Early emergence of cortical interneuron diversity in the mouse embryo. *Science*, 360(6384):81–85.

Miyoshi, G., Butt, S. J. B., Takebayashi, H., and Fishell, G. (2007). Physiologically distinct temporal cohorts of cortical interneurons arise from telencephalic olig2-expressing precursors. *J Neurosci*, 27(29):7786–98.

Miyoshi, G. and Fishell, G. (2011). Gabaergic interneuron lineages selectively sort into specific cortical layers during early postnatal development. *Cereb Cortex*, 21(4):845–52.

Monory, K., Massa, F., Egertová, M., Eder, M., Blaudzun, H., Westenbroek, R., Kelsch, W., Jacob, W., Marsch, R., Ekker, M., Long, J., Rubenstein, J. L., Goebbels, S., Nave, K.-A., During, M., Klugmann, M., Wölfel, B., Dodt, H.-U., Zieglgänsberger, W., Wotjak, C. T., Mackie, K., Elphick, M. R., Marsicano, G., and Lutz, B. (2006). The endocannabinoid system controls key epileptogenic circuits in the hippocampus. *Neuron*, 51(4):455–66.

Moreau, M. X., Saillour, Y., Cwetsch, A. W., Pierani, A., and Causeret, F. (2021). Single-cell transcriptomics of the early developing mouse cerebral cortex disentangle the spatial and temporal components of neuronal fate acquisition. *Development*, 148(14).

Nery, S., Fishell, G., and Corbin, J. G. (2002). The caudal ganglionic eminence is a source of distinct cortical and subcortical cell populations. *Nat Neurosci*, 5(12):1279–87.

Nishino, J., Kim, I., Chada, K., and Morrison, S. J. (2008). Hmga2 Promotes Neural Stem Cell Self-Renewal in Young but Not Old Mice by Reducing p16Ink4a and p19Arf Expression. *Cell*, 135(2):227–239. Publisher: Elsevier.

Oberst, P., Fièvre, S., Baumann, N., Concetti, C., Bartolini, G., and Jabaudon, D. (2019). Temporal plasticity of apical progenitors in the developing mouse neocortex. *Nature*, 573(7774):370–374.

Ohtsuka, T., Sakamoto, M., Guillemot, F., and Kageyama, R. (2001). Roles of the Basic Helix-Loop-Helix Genes Hes1 and Hes5 in Expansion of Neural Stem Cells of the Developing Brain. *Journal of Biological Chemistry*, 276(32):30467–30474.

Petros, T. J., Bultje, R. S., Ross, M. E., Fishell, G., and Anderson, S. A. (2015). Apical versus basal neurogenesis directs cortical interneuron subclass fate. *Cell Rep*, 13(6):1090–1095.

Piper, M., Barry, G., Harvey, T. J., McLeay, R., Smith, A. G., Harris, L., Mason, S., Stringer, B. W., Day, B. W., Wray, N. R., Gronostajski, R. M., Bailey, T. L., Boyd, A. W., and Richards, L. J. (2014). Nfib-mediated repression of the epigenetic factor ezh2 regulates cortical development. *J Neurosci*, 34(8):2921–30.

Pipicelli, F., Baumann, N., Di Giaimo, R., Forero-Echeverry, A., Kyrousi, C., Bonrath, R., Maccarrone, G., Jabaudon, D., and Cappello, S. (2023). Non-cell-autonomous regulation of interneuron specification mediated by extracellular vesicles. *Sci Adv*, 9(20):eadd8164.

Pjanic, M., Schmid, C. D., Gaussin, A., Ambrosini, G., Adamcik, J., Pjanic, P., Plasari, G., Kerschgens, J., Dietler, G., Bucher, P., and Mermod, N. (2013). Nuclear factor i genomic binding associates with chromatin boundaries. *BMC Genomics*, 14:99.

Puelles, L., Kuwana, E., Puelles, E., Bulfone, A., Shimamura, K., Keleher, J., Smiga, S., and Rubenstein, J. L. (2000). Pallial and subpallial derivatives in the embryonic chick and mouse telencephalon, traced by the expression of the genes dlx-2, emx-1, nkx-2.1, pax-6, and tbr-1. *J Comp Neurol*, 424(3):409–38.

Qiu, X., Mao, Q., Tang, Y., Wang, L., Chawla, R., Pliner, H. A., and Trapnell, C. (2017). Reversed graph embedding resolves complex single-cell trajectories. *Nature Methods*, 14(10):979–982.

Raposo, A. A. S. F., Vasconcelos, F. F., Drechsel, D., Marie, C., Johnston, C., Dolle, D., Bithell, A., Gillotin, S., van den Berg, D. L. C., Ettwiller, L., Flicek, P., Crawford, G. E., Parras, C. M.,

Berninger, B., Buckley, N. J., Guillemot, F., and Castro, D. S. (2015). Ascl1 Coordinately Regulates Gene Expression and the Chromatin Landscape during Neurogenesis. *Cell Reports*, 10(9):1544–1556.

Reillo, I., de Juan Romero, C., Cárdenas, A., Clascá, F., Martínez-Martinez, M. Á., and Borrell, V. (2017). A complex code of extrinsic influences on cortical progenitor cells of higher mammals. *Cereb Cortex*, 27(9):4586–4606.

Rhodes, C. T., Thompson, J. J., Mitra, A., Asokumar, D., Lee, D. R., Lee, D. J., Zhang, Y., Jason, E., Dale, R. K., Rocha, P. P., and Petros, T. J. (2022). An epigenome atlas of neural progenitors within the embryonic mouse forebrain. *Nat Commun*, 13(1):4196.

Rubenstein, J. L. and Puelles, L. (1994). Homeobox gene expression during development of the vertebrate brain. *Curr Top Dev Biol*, 29:1–63.

Ryu, Y., Iwashita, M., Lee, W., Uchimura, K., and Kosodo, Y. (2021). A shift in tissue stiffness during hippocampal maturation correlates to the pattern of neurogenesis and composition of the extracellular matrix. *Front Aging Neurosci*, 13:709620.

Sandberg, M., Flandin, P., Silberberg, S., Su-Feher, L., Price, J. D., Hu, J. S., Kim, C., Visel, A., Nord, A. S., and Rubenstein, J. L. R. (2016). Transcriptional networks controlled by nkx2-1 in the development of forebrain gabaergic neurons. *Neuron*, 91(6):1260–1275.

Satpathy, A. T., Granja, J. M., Yost, K. E., Qi, Y., Meschi, F., McDermott, G. P., Olsen, B. N., Mumbach, M. R., Pierce, S. E., Corces, M. R., Shah, P., Bell, J. C., Jhutty, D., Nemec, C. M., Wang, J., Wang, L., Yin, Y., Giresi, P. G., Chang, A. L. S., Zheng, G. X. Y., Greenleaf, W. J., and Chang, H. Y. (2019). Massively parallel single-cell chromatin landscapes of human immune cell development and intratumoral T cell exhaustion. *Nature Biotechnology*, 37(8):925–936. Number: 8 Publisher: Nature Publishing Group.

Shimamura, K., Hartigan, D. J., Martinez, S., Puelles, L., and Rubenstein, J. L. (1995). Longitudinal organization of the anterior neural plate and neural tube. *Development*, 121(12):3923–33.

Stuart, T., Butler, A., Hoffman, P., Hafemeister, C., Papalexi, E., Mauck, W. M., Hao, Y., Stoeckius, M., Smibert, P., and Satija, R. (2019). Comprehensive Integration of Single-Cell Data. *Cell*, 177(7):1888–1902.e21. Publisher: Elsevier.

Su, Z., Wang, Z., Lindtner, S., Yang, L., Shang, Z., Tian, Y., Guo, R., You, Y., Zhou, W., Rubenstein, J. L., Yang, Z., and Zhang, Z. (2022). Dlx1/2-dependent expression of meis2 promotes neuronal fate determination in the mammalian striatum. *Development*, 149(4).

Taniguchi, H., He, M., Wu, P., Kim, S., Paik, R., Sugino, K., Kvitsiani, D., Fu, Y., Lu, J., Lin, Y., Miyoshi, G., Shima, Y., Fishell, G., Nelson, S. B., and Huang, Z. J. (2011). A resource of cre driver lines for genetic targeting of gabaergic neurons in cerebral cortex. *Neuron*, 71(6):995–1013.

Telley, L., Agirman, G., Prados, J., Amberg, N., Fièvre, S., Oberst, P., Bartolini, G., Vitali, I., Cadilhac, C., Hippenmeyer, S., Nguyen, L., Dayer, A., and Jabaudon, D. (2019). Temporal patterning of apical progenitors and their daughter neurons in the developing neocortex. *Science*, 364(6440).

Telley, L., Govindan, S., Prados, J., Stevant, I., Nef, S., Dermitzakis, E., Dayer, A., and Jabaudon, D. (2016). Sequential transcriptional waves direct the differentiation of newborn neurons in the mouse neocortex. *Science*, 351(6280):1443–6.

Thakurela, S., Tiwari, N., Schick, S., Garding, A., Ivanek, R., Berninger, B., and Tiwari, V. K. (2016). Mapping gene regulatory circuitry of Pax6 during neurogenesis. *Cell Discovery*, 2(1):1–22. Number: 1 Publisher: Nature Publishing Group.

Tirosh, I., Izar, B., Prakadan, S. M., Wadsworth, M. H., Treacy, D., Trombetta, J. J., Rotem, A., Rodman, C., Lian, C., Murphy, G., Fallahi-Sichani, M., Dutton-Regester, K., Lin, J.-R., Cohen, O., Shah, P., Lu, D., Genshaft, A. S., Hughes, T. K., Ziegler, C. G. K., Kazer, S. W., Gaillard, A., Kolb, K. E., Villani, A.-C., Johannessen, C. M., Andreev, A. Y., Van Allen, E. M., Bertagnolli, M., Sorger, P. K., Sullivan, R. J., Flaherty, K. T., Frederick, D. T., Jané-Valbuena, J., Yoon, C. H., Rozenblatt-Rosen, O., Shalek, A. K., Regev, A., and Garraway, L. A. (2016). Dissecting the multicellular ecosystem of metastatic melanoma by single-cell RNA-seq. *Science*, 352(6282):189–196. Publisher: American Association for the Advancement of Science.

Trapnell, C., Cacchiarelli, D., Grimsby, J., Pokharel, P., Li, S., Morse, M., Lennon, N. J., Livak, K. J., Mikkelsen, T. S., and Rinn, J. L. (2014). The dynamics and regulators of cell fate decisions are revealed by pseudotemporal ordering of single cells. *Nat Biotechnol*, 32(4):381–386.

van Heusden, F., Macey-Dare, A., Gordon, J., Krajeski, R., Sharott, A., and Ellender, T. (2021). Diversity in striatal synaptic circuits arises from distinct embryonic progenitor pools in the ventral telencephalon. *Cell Rep*, 35(4):109041.

Vitali, I., Fièvre, S., Telley, L., Oberst, P., Bariselli, S., Frangeul, L., Baumann, N., McMahon, J. J., Klingler, E., Bocchi, R., Kiss, J. Z., Bellone, C., Silver, D. L., and Jabaudon, D. (2018). Progenitor hyperpolarization regulates the sequential generation of neuronal subtypes in the developing neocortex. *Cell*, 174(5):1264–1276.e15.

Wagner, D. E., Weinreb, C., Collins, Z. M., Briggs, J. A., Megason, S. G., and Klein, A. M. (2018). Single-cell mapping of gene expression landscapes and lineage in the zebrafish embryo. *Science*, 360(6392):981–987. Publisher: American Association for the Advancement of Science.

Wang, Y., Liu, L., and Lin, M. (2022). Psychiatric risk gene transcription factor 4 preferentially regulates cortical interneuron neurogenesis during early brain development. *J Biomed Res*, 36(4):242–254.

Wichterle, H., Turnbull, D. H., Nery, S., Fishell, G., and Alvarez-Buylla, A. (2001). In utero fate mapping reveals distinct migratory pathways and fates of neurons born in the mammalian basal forebrain. *Development*, 128(19):3759–71.

Wonders, C. P. and Anderson, S. A. (2006). The origin and specification of cortical interneurons. *Nat Rev Neurosci*, 7(9):687–96.

Wonders, C. P., Taylor, L., Welagen, J., Mbata, I. C., Xiang, J. Z., and Anderson, S. A. (2008). A spatial bias for the origins of interneuron subgroups within the medial ganglionic eminence. *Dev Biol*, 314(1):127–36.

Wu, Q., Shichino, Y., Abe, T., Suetsugu, T., Omori, A., Kiyonari, H., Iwasaki, S., and Matsuzaki, F. (2022). Selective translation of epigenetic modifiers affects the temporal pattern and differentiation of neural stem cells. *Nat Commun*, 13(1):470.

Xu, Q., Cobos, I., De La Cruz, E., Rubenstein, J. L., and Anderson, S. A. (2004). Origins of cortical interneuron subtypes. *J Neurosci*, 24(11):2612–22.

Yoon, K.-J., Vissers, C., Ming, G.-L., and Song, H. (2018). Epigenetics and epitranscriptomics in temporal patterning of cortical neural progenitor competence. *J Cell Biol*, 217(6):1901–1914.

Zenker, M., Bunt, J., Schanze, I., Schanze, D., Piper, M., Priolo, M., Gerkes, E. H., Gronostajski, R. M., Richards, L. J., Vogt, J., Wessels, M. W., and Hennekam, R. C. (2019). Variants in nuclear factor i genes influence growth and development. *Am J Med Genet C Semin Med Genet*, 181(4):611–626.

Zhang, Y., Liu, T., Meyer, C. A., Eeckhoute, J., Johnson, D. S., Bernstein, B. E., Nusbaum, C., Myers, R. M., Brown, M., Li, W., and Liu, X. S. (2008). Model-based Analysis of ChIP-Seq (MACS). *Genome Biology*, 9(9):R137.

Zheng, G. X. Y., Terry, J. M., Belgrader, P., Ryvkin, P., Bent, Z. W., Wilson, R., Ziraldo, S. B., Wheeler, T. D., McDermott, G. P., Zhu, J., Gregory, M. T., Shuga, J., Montesclaros, L., Underwood, J. G., Masquelier, D. A., Nishimura, S. Y., Schnall-Levin, M., Wyatt, P. W., Hindson, C. M., Bharadwaj, R., Wong, A., Ness, K. D., Beppu, L. W., Deeg, H. J., McFarland, C., Loeb, K. R., Valente, W. J., Ericson, N. G., Stevens, E. A., Radich, J. P., Mikkelsen, T. S., Hindson, B. J., and Bielas, J. H. (2017). Massively parallel digital transcriptional profiling of single cells. *Nature Communications*, 8(1):14049. Number: 1 Publisher: Nature Publishing Group.

Zong, N., Wang, M., Fu, Y., Shen, D., and Yu, Y.-C. (2022). Cell-cycle length of medial ganglionic eminence progenitors contributes to interneuron fate. *Protein Cell*, 13(2):141–147.